







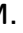
























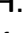




















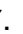










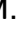













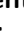

















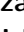














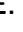




























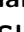



















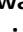




































Measurement of the energy dependence of the $e^+e^- \rightarrow B\bar{B}, B\bar{B}^*$, and $B^*\bar{B}^*$ cross sections at Belle II

The Belle II collaboration

I. Adachi , L. Aggarwal , H. Ahmed , H. Aihara , N. Akopov , A. Aloisio , N. Althubiti , N. Anh Ky , D. M. Asner , H. Atmacan , T. Aushev , V. Aushev , M. Aversano , R. Ayad , V. Babu , H. Bae , S. Bahinipati , P. Bambade , Sw. Banerjee , S. Bansal , M. Barrett , J. Baudot , M. Bauer , A. Baur , A. Beaubien , F. Becherer , J. Becker , P. K. Behera , J. V. Bennett , F. U. Bernlochner , V. Bertacchi , M. Bertemes , E. Bertholet , M. Bessner , S. Bettarini , B. Bhuyan , F. Bianchi , L. Bierwirth , T. Bilka , D. Biswas , A. Bobrov , D. Bodrov , A. Bolz , A. Bondar , J. Borah , A. Boschetti , A. Bozek , M. Bračko , P. Branchini , R. A. Briere , T. E. Browder , A. Budano , S. Bussino , Q. Campagna , M. Campajola , L. Cao , G. Casarosa , C. Cecchi , J. Cerasoli , M.-C. Chang , P. Chang , P. Cheema , B. G. Cheon , K. Chilikin , K. Chirapatpimol , H.-E. Cho , K. Cho , S.-J. Cho , S.-K. Choi , S. Choudhury , J. Cochran , L. Corona , J. X. Cui , S. Das , F. Dattola , E. De La Cruz-Burelo , S. A. De La Motte , G. de Marino , G. De Nardo , M. De Nuccio , G. De Pietro , R. de Sangro , M. Destefanis , S. Dey , R. Dhamija , A. Di Canto , F. Di Capua , J. Dingfelder , Z. Doležal , I. Domínguez Jiménez , T. V. Dong , M. Dorigo , D. Dorner , K. Dort , D. Dossett , S. Dreyer , S. Dubey , K. Dugic , G. Dujany , P. Ecker , M. Eliachevitch , D. Epifanov , P. Feichtinger , T. Ferber , D. Ferlewicz , T. Fillinger , C. Finck , G. Finocchiaro , A. Fodor , F. Forti , A. Frey , B. G. Fulsom , A. Gabrielli , E. Ganiev , M. Garcia-Hernandez , R. Garg , A. Garmash , G. Gaudino , V. Gaur , A. Gaz , A. Gellrich , G. Ghevondyan , D. Ghosh , H. Ghumaryan , G. Giakoustidis , R. Giordano , A. Giri , A. Glazov , B. Gobbo , R. Godang , O. Gogota , P. Goldenzweig , W. Gradl , T. Grammatico , S. Granderath , E. Graziani , D. Greenwald , Z. Gruberová , T. Gu , Y. Guan , K. Gudkova , S. Halder , Y. Han , K. Hara , T. Hara , C. Harris , K. Hayasaka , H. Hayashii , S. Hazra , C. Hearty , M. T. Hedges , A. Heidelberg , I. Heredia de la Cruz , M. Hernández Villanueva , A. Hershenhorn , T. Higuchi , E. C. Hill , M. Hoek , M. Hohmann , P. Horak , C.-L. Hsu , T. Humair , T. Iijima , K. Inami , G. Inguglia , N. Ipsita , A. Ishikawa , S. Ito , R. Itoh

M. Iwasaki , P. Jackson , W. W. Jacobs , E.-J. Jang , Q. P. Ji , S. Jia ,
Y. Jin , A. Johnson , K. K. Joo , H. Junkerkalefeld , H. Kakuno , M. Kaleta ,
D. Kalita , A. B. Kaliyar , J. Kandra , K. H. Kang , S. Kang , G. Karyan ,
T. Kawasaki , F. Keil , C. Ketter , C. Kiesling , C.-H. Kim , D. Y. Kim ,
K.-H. Kim , Y.-K. Kim , H. Kindo , K. Kinoshita , P. Kodyš , T. Koga ,
S. Kohani , K. Kojima , T. Konno , A. Korobov , S. Korpar , E. Kovalenko ,
R. Kowalewski , T. M. G. Kraetzschmar , P. Križan , P. Krokovny , Y. Kulii ,
T. Kuhr , J. Kumar , M. Kumar , R. Kumar , K. Kumara , T. Kunigo ,
A. Kuzmin , Y.-J. Kwon , S. Lacaprara , Y.-T. Lai , T. Lam , L. Lanceri ,
J. S. Lange , M. Laurenza , R. Leboucher , F. R. Le Diberder , M. J. Lee ,
P. Leitl , P. Leo , D. Levit , P. M. Lewis , C. Li , L. K. Li , S. X. Li , Y. Li ,
Y. B. Li , J. Libby , Q. Y. Liu , Z. Q. Liu , D. Liventsev , S. Longo ,
A. Lozar , T. Lueck , C. Lyu , Y. Ma , M. Maggiora , S. P. Maharana ,
R. Maiti , S. Maity , G. Mancinelli , R. Manfredi , E. Manoni ,
M. Mantovano , D. Marcantonio , S. Marcello , C. Marinas , L. Martel ,
C. Martellini , A. Martini , T. Martinov , L. Massaccesi , M. Masuda ,
T. Matsuda , K. Matsuoka , D. Matvienko , S. K. Maurya , J. A. McKenna ,
R. Mehta , F. Meier , M. Merola , F. Metzner , M. Milesi , C. Miller ,
M. Mirra , S. Mitra , K. Miyabayashi , H. Miyake , R. Mizuk , G. B. Mohanty ,
N. Molina-Gonzalez , S. Mondal , S. Moneta , H.-G. Moser , M. Mrvar ,
R. Mussa , I. Nakamura , M. Nakao , Y. Nakazawa , A. Narimani Charan ,
M. Naruki , D. Narwal , Z. Natkaniec , A. Natochii , L. Nayak , M. Nayak ,
G. Nazaryan , M. Neu , C. Niebuhr , N. K. Nisar , S. Nishida , S. Ogawa ,
Y. Onishchuk , H. Ono , Y. Onuki , P. Oskin , F. Otani , P. Pakhlov ,
G. Pakhlova , A. Paladino , A. Panta , E. Paoloni , S. Pardi , K. Parham ,
H. Park , J. Park , S.-H. Park , B. Paschen , A. Passeri , S. Patra , S. Paul ,
T. K. Pedlar , I. Peruzzi , R. Peschke , R. Pestotnik , F. Pham , M. Piccolo ,
L. E. Piilonen , G. Pinna Angioni , P. L. M. Podesta-Lerma , T. Podobnik ,
S. Pokharel , C. Praz , S. Prell , E. Prencipe , M. T. Prim , S. Privalov ,
H. Purwar , N. Rad , P. Rados , G. Raeuber , S. Raiz , N. Rauls ,
K. Ravindran , M. Reif , S. Reiter , M. Remnev , L. Reuter , I. Ripp-Baudot ,
S. H. Robertson , M. Roehrken , J. M. Roney , A. Rostomyan , N. Rout ,
G. Russo , D. Sahoo , D. A. Sanders , S. Sandilya , A. Sangal , L. Santelj ,
Y. Sato , V. Savinov , B. Scavino , S. Schneider , M. Schnepf , C. Schwanda ,
Y. Seino , A. Selce , K. Senyo , J. Serrano , M. E. Sevior , C. Sfienti ,
W. Shan , C. Sharma , C. P. Shen , X. D. Shi , T. Shillington , T. Shimasaki ,
J.-G. Shiu , D. Shtol , B. Shwartz , A. Sibidanov , F. Simon , J. B. Singh ,
J. Skorupa , K. Smith , R. J. Sobie , M. Sobotzik , A. Soffer , A. Sokolov ,
E. Solovieva , S. Spataro , B. Spruck , M. Starič , P. Stavroulakis ,
S. Stefkova , Z. S. Stottler , R. Stroili , J. Strube , Y. Sue , M. Sumihama ,
K. Sumisawa , W. Sutcliffe , H. Svidras , M. Takahashi , M. Takizawa ,
U. Tamponi , S. Tanaka , K. Tanida , F. Tenchini , A. Thaller , O. Tittel ,
R. Tiwary , D. Tonelli , E. Torassa , N. Toutounji , K. Trabelsi , I. Tsaklidis

M. Uchida , I. Ueda , Y. Uematsu , T. Uglov , K. Unger , Y. Unno , K. Uno ,
S. Uno , P. Urquijo , Y. Ushiroda , S. E. Vahsen , R. van Tonder ,
G. S. Varner , K. E. Varvell , M. Veronesi , A. Vinokurova , V. S. Vismaya ,
L. Vitale , V. Vobbilisetti , R. Volpe , B. Wach , M. Wakai , S. Wallner ,
E. Wang , M.-Z. Wang , X. L. Wang , Z. Wang , A. Warburton ,
M. Watanabe , S. Watanuki , C. Wessel , E. Won , X. P. Xu , B. D. Yabsley ,
S. Yamada , W. Yan , S. B. Yang , J. Yelton , J. H. Yin , K. Yoshihara ,
C. Z. Yuan , L. Zani , F. Zeng , B. Zhang , Y. Zhang , V. Zhilich ,
J. S. Zhou , Q. D. Zhou , X. Y. Zhou , V. I. Zhukova , R. Žlebčik 

ABSTRACT: We report measurements of the $e^+e^- \rightarrow B\bar{B}$, $B\bar{B}^*$, and $B^*\bar{B}^*$ cross sections at four energies, 10653, 10701, 10746 and 10805 MeV, using data collected by the Belle II experiment. We reconstruct one B meson in a large number of hadronic final states and use its momentum to identify the production process. In the first 2 – 5 MeV above $B^*\bar{B}^*$ threshold, the $e^+e^- \rightarrow B^*\bar{B}^*$ cross section increases rapidly. This may indicate the presence of a pole close to the threshold.

KEYWORDS: e^+e^- Experiments, Quarkonium, Spectroscopy

Contents

1	Introduction	1
2	Belle II detector and data sets	3
3	Event selection	4
4	Simulation studies and corrections	7
4.1	Calibration of simulation	7
4.2	Optimization	7
4.3	Dependence of the FEI efficiency on E_{cm}	7
5	Absolute value of the FEI efficiency	8
5.1	Momentum resolution	9
5.2	Backgrounds and broken signal	9
5.3	Fit to the $\Upsilon(4S)$ data	11
5.3.1	Systematic uncertainties at the $\Upsilon(4S)$	12
5.4	Determination of the FEI efficiency at the $\Upsilon(4S)$	14
6	Measurements at the scan energies	14
6.1	M_{bc} fits at scan energies	15
6.2	Fit to the energy dependence of the cross sections	19
6.3	Systematic uncertainties	20
7	Discussion and summary	23
8	Acknowledgements	26
A	Reconstruction channels of B and D mesons	29

1 Introduction

All known hadrons that contain a heavy $b\bar{b}$ quark pair and have mass above the open bottom ($B\bar{B}$) threshold, $\Upsilon(4S)$, $\Upsilon(10860)$, and $\Upsilon(11020)$, exhibit anomalous properties [1]. In particular, the $\pi^+\pi^-$ transitions to lower bottomonium levels are strongly enhanced compared to similar transitions from below-threshold states, and the η transitions are not strongly suppressed compared to the $\pi^+\pi^-$ transitions; the latter property violates heavy-quark spin symmetry. These unexpected properties could be explained if the hadrons have an exotic admixture: for example, in addition to $b\bar{b}$, they may also contain multiquark $b\bar{b}q\bar{q}$ or hybrid $b\bar{b}g$ components, where q and g represent a valence light quark and valence gluon, respectively [2–5].

In 2019, the Belle experiment observed a new structure, $\Upsilon(10753)$, in the energy dependence of the $e^+e^- \rightarrow \Upsilon(nS)\pi^+\pi^-$ ($n = 1, 2, 3$) cross sections [6]. While the global significance of the observation is 5.2 standard deviations, an independent confirmation would be important. There is a dip in the total $b\bar{b}$ cross section at the position of the new state, which could be due to destructive interference with other contributions [7].

Recently, the Belle experiment measured the energy dependence of the $e^+e^- \rightarrow B\bar{B}$, $B\bar{B}^*$, and $B^*\bar{B}^*$ cross sections [8]. These open-flavor final states are expected to be the dominant decay channels for $b\bar{b}$ hadrons and constitute the main contribution to the total $b\bar{b}$ cross section. In fact, their measurement enabled a combined analysis of all available energy-scan results [9]. The following cross sections were considered: $e^+e^- \rightarrow B\bar{B}$, $B\bar{B}^*$, $B^*\bar{B}^*$, $B_s^{(*)}\bar{B}_s^{(*)}$, $\Upsilon(nS)\pi^+\pi^-$ ($n = 1, 2, 3$), $h_b(mP)\pi^+\pi^-$ ($m = 1, 2$), and the total $b\bar{b}$ cross section. The coupled-channel approach was used, which takes into account rescattering between different channels. The results of the combined analysis were the pole positions of the Υ resonances and the energy dependence of the scattering amplitudes. The combined analysis provided further confirmation of the $\Upsilon(10753)$ state. However, its pole position has large uncertainty. In addition, the scattering amplitudes have large uncertainties in the $\Upsilon(10753)$ region where the spacing between the Belle scan points is large, about 50 MeV.

In order to improve understanding of the $\Upsilon(10753)$ energy region, the SuperKEKB collider performed an energy scan in November 2021. Four data samples have been collected by the Belle II experiment; corresponding center-of-mass (c.m.) energies and integrated luminosities are shown in Table 1. The energies have been chosen to fill the gaps between

Table 1: Center-of-mass energy and integrated luminosity of the scan data samples. The uncertainties in the c.m. energy shown here are uncorrelated point-to-point; the correlated uncertainty is 0.5 MeV. The uncorrelated uncertainty in the luminosity is negligibly small; the correlated uncertainty is 0.6%.

Point#	E_{cm} (MeV)	L (fb $^{-1}$)
1	10804.50 ± 0.70	4.690
2	10746.30 ± 0.48	9.818
3	10700.90 ± 0.63	1.633
4	10653.30 ± 1.14	3.521

the Belle scan points. The integrated luminosities are larger than those at Belle, which are approximately 1 fb $^{-1}$ per point. The largest sample is collected at the expected $\Upsilon(10753)$ peak position so that $\Upsilon(10753)$ decays can be studied. Using these data, Belle II measured the $e^+e^- \rightarrow \Upsilon(nS)\pi^+\pi^-$ ($n = 1, 2, 3$) cross sections, confirming the $\Upsilon(10753)$ state with high significance [10]; observed a strong enhancement of the $e^+e^- \rightarrow \chi_{bJ}(1P)\omega$ ($J = 1, 2$) cross sections in the $\Upsilon(10753)$ region, establishing the $\Upsilon(10753) \rightarrow \chi_{b1}(1P)\omega$ decay channel [11]; and set stringent upper limits on the $e^+e^- \rightarrow \eta_b(1S)\omega$ and $e^+e^- \rightarrow \chi_{b0}(1P)\omega$ cross sections near the $\Upsilon(10753)$ peak [12].

In this paper, we report measurements of the $e^+e^- \rightarrow B\bar{B}$, $B\bar{B}^*$, and $B^*\bar{B}^*$ cross

sections using the scan data collected by Belle II. Our analysis closely follows that of Belle [8]. We perform a full reconstruction of one B meson in hadronic channels, and then identify the $B\bar{B}$, $B\bar{B}^*$, and $B^*\bar{B}^*$ signals using the M_{bc} distribution,

$$M_{bc} = \sqrt{(E_{\text{cm}}/2)^2 - p_B^2}, \quad (1.1)$$

where E_{cm} is the c.m. energy of the colliding beams and p_B is the B -candidate momentum in the c.m. frame. In all equations in this paper, we use natural units $c = 1$. The M_{bc} variable is essentially a transformation of the B -meson momentum that provides a simpler parametrization of the background near the kinematic end-point. Photons from $B^* \rightarrow B\gamma$ decays are not reconstructed. To reconstruct B mesons in a large number of hadronic final states, we apply the multivariate full event interpretation (FEI) algorithm [13]. We use an FEI configuration optimized for energy-scan analyses [8]. The optimization primarily concerns FEI inputs, which are chosen to make the reconstruction efficiency independent of energy. The ΔE variable is not included in the training and a sideband in the $(M_{bc}, \Delta E)$ plane is used to constrain backgrounds. The ΔE variable is defined as

$$\Delta E = E_B - E_{\text{cm}}/2, \quad (1.2)$$

where E_B is the B -candidate energy measured in the c.m. frame. The absolute value of the reconstruction efficiency is determined using $\Upsilon(4S)$ data. In the M_{bc} fits, the signals are described using a function developed in Ref. [8] that is calculated numerically and includes all relevant effects, in particular, initial-state radiation (ISR) and the energy dependence of the cross sections. The latter is determined by fitting both the cross sections measured in this analysis and the results of the Belle measurement [8]. To obtain self-consistent results, an iterative procedure is used.

The paper is organized as follows. We describe the Belle II detector and data sets in Section 2. The selection of events using the FEI is presented in Section 3. We discuss the calibration of the Monte Carlo (MC) simulation, optimization of the final selection requirements, and determination of the dependence of the FEI efficiency on c.m. energy in Section 4. Section 5 is devoted to the measurement of the absolute value of the FEI efficiency using $\Upsilon(4S)$ data. The fits to M_{bc} at the scan energies, the fit to the energy dependence of the $B^{(*)}\bar{B}^{(*)}$ cross sections, and the evaluation of the systematic uncertainties are described in Section 6. Discussion of the results and summary are in Section 7.

2 Belle II detector and data sets

The analysis is based on the data collected by the Belle II detector [14] operating at the SuperKEKB asymmetric-energy e^+e^- collider [15] at KEK.

The Belle II detector is a cylindrical large-solid-angle magnetic spectrometer consisting of a silicon pixel detector surrounded by a four-layer double-sided silicon strip detector (SVD) and a 56-layer central drift chamber (CDC) providing information about charged particle trajectories (tracks) and vertex positions. Surrounding the CDC, a time-of-propagation counter (TOP) in the barrel region and an aerogel-based ring-imaging Cherenkov counter

(ARICH) in the endcap region provide charged-particle identification (PID). Surrounding the TOP and ARICH, an electromagnetic calorimeter based on CsI(Tl) crystals provides energy and timing measurements for photons and electrons. These sub-systems are surrounded by a superconducting solenoid, providing an axial magnetic field of 1.5 T. An iron flux return located outside the coil is instrumented with resistive plate chambers and plastic scintillators to detect K_L^0 mesons and to identify muons (KLM). More details about the detector are given in Ref. [14].

The z axis of the Belle II detector is defined as the symmetry axis of the solenoid, and the positive direction is approximately given by the electron-beam direction. The polar angle θ , as well as the longitudinal and the transverse directions, are defined with respect to the z axis.

The data analysis strategy is tested on simulated event samples. Events containing B mesons are generated using the EvtGen package [16]. Continuum $e^+e^- \rightarrow q\bar{q}$ background processes, where $q = u, d, s, c$, are generated with KKMC [17] and PYTHIA 8 [18]. Final-state radiation of photons from stable charged particles is simulated with PHOTOS [19]. The detector response and K_S^0 decays are simulated using Geant4 [20]. Both collision data and simulated samples are processed using the Belle II software [21].

We use the Belle II energy-scan data, consisting of the four samples with energies and luminosities shown in Table 1. To determine the FEI efficiency, we use $\Upsilon(4S)$ data taken immediately before and after the energy scan period; the combined integrated luminosity of this $\Upsilon(4S)$ data sample is 35.5 fb^{-1} .

3 Event selection

In the configuration of the FEI used here (following [8]), we reconstruct the B^+ and B^0 mesons in the decay channels $\bar{D}^{(*)}\pi^+(\pi^+\pi^-)$, $D_s^{(*)+}\bar{D}^{(*)}$, $J/\psi K^+(\pi^-)$, $J/\psi K_S^0(\pi^+)$, $J/\psi K_S^0\pi^+\pi^-$, $D^{(*)-}\pi^+\pi^+$, and $D^{*-}K^+K^-\pi^+$, where \bar{D} denotes the \bar{D}^0 and D^- mesons.¹ The D^0 , D^+ , and D_s^+ mesons are reconstructed in final states with K^\pm , K_S^0 , π^\pm , up to one π^0 , and multiplicity up to five. The list of channels that are used for reconstruction of B and D mesons is presented in Appendix A. We reconstruct D^* mesons in the $D\pi$ and $D\gamma$ channels; J/ψ are reconstructed in the $\mu^+\mu^-$ and e^+e^- final states.

We perform a loose selection of the final-state particles and decays, and subsequently use multivariate analysis for the final selection. We select tracks that originate from the vicinity of the interaction point (IP) by imposing $dr < 0.5 \text{ cm}$ and $dz < 3 \text{ cm}$, where dr and dz are transverse and longitudinal distances between the track and the IP. The PID is based on the ionization energy-loss measurement in the CDC and responses of the TOP, ARICH, ECL, and KLM. Information from these subdetectors is combined into a likelihood \mathcal{L}_h for a given hypothesis h [22], and the ratio $R_h = \mathcal{L}_h / (\mathcal{L}_{e^+} + \mathcal{L}_{\mu^+} + \mathcal{L}_{\pi^+} + \mathcal{L}_{K^+} + \mathcal{L}_p + \mathcal{L}_d)$ is used in the selection. In the initial selection, we apply the PID requirement only for kaon candidates, $R_{K^+} > 0.1$. The efficiency of this requirement is 86% and the probability to misidentify a pion as a kaon is about 7%. We require photons to have energies greater than 100, 90, and 160 MeV in the forward endcap ($12.4^\circ < \theta < 31.4^\circ$), barrel ($32.2^\circ < \theta <$

¹Throughout this paper, charge conjugated channels are always included.

128.7°), and backward endcap ($130.7^\circ < \theta < 155.1^\circ$) regions of the ECL, respectively, as the backgrounds in these regions are different. For the K_S^0 , π^0 , D , and J/ψ candidates, we apply a loose mass-range requirement that corresponds to about ± 5 units of mass resolution. For the D^* candidates, we use the mass difference $M(D^*) - M(D)$. To improve momentum resolution, we apply a mass-constrained fit to π^0 , J/ψ , and D^* candidates; a mass-vertex-constrained fit to D and D_s^+ ; and a vertex-constrained fit to K_S^0 and B .

A boosted decision tree [23] is used with the following discriminating variables for various particle species.

- For charged pions, kaons, and leptons, we use the laboratory momentum, the transverse momentum, and the PID information, which consists of likelihood ratios for the e^+ , μ^+ , π^+ , K^+ , and p hypotheses.
- For photons, we use the laboratory momentum, the polar angle, the number of crystals in the energy deposition (cluster), the ratio of the energy deposition in a 3×3 matrix of crystals to that in a 5×5 matrix without corner crystals, and the cluster timing. These variables are used to suppress hadron showers and beam background.
- For $K_S^0 \rightarrow \pi^+\pi^-$ candidates, we use the invariant mass and laboratory momentum of the K_S^0 candidate, the distance between the IP and the K_S^0 vertex, the cosine of the angle between the K_S^0 momentum and the direction from the IP to the K_S^0 vertex, the distance between the π^+ and π^- tracks along the beam direction at the K_S^0 vertex, the numbers of SVD and CDC measurement points (hits) of π^+ and π^- , and the decay angle (the angle between the π^+ momentum measured in the K_S^0 rest frame and the K_S^0 boost direction from the laboratory frame).
- For $\pi^0 \rightarrow \gamma\gamma$ candidates, we use the invariant mass, the laboratory momentum of the π^0 candidate, and its decay angle.
- For D meson candidates, we use the invariant mass and p-value of the mass-vertex constrained fit. In three-body decays, we include invariant masses of intermediate $\rho(\rightarrow \pi\pi)$, $K^*(\rightarrow K\pi)$, and $\phi(\rightarrow K^+K^-)$ resonance candidates.
- For J/ψ and D^* candidates we use invariant masses.
- For B meson candidates, we use the p-value of the vertex-constrained fit. If there is a D meson in the decay, we include the distance between the B and D vertices, this distance divided by its uncertainty, and the cosine of the angle between the D momentum and the direction from the B to the D vertex. If there are several pions or kaons in the decay, we include invariant masses of intermediate ρ , K^* , and $a_1(\rightarrow \pi\pi\pi)$ resonance candidates.
- To suppress continuum $e^+e^- \rightarrow q\bar{q}$ backgrounds, where q denotes a u , d , s , or c quark, we use the event-shape variable R_2 (the ratio of the second to zeroth Fox-Wolfram moments [24]), the angle between the thrust axes of the B candidate and the rest of the event [22], and two boolean variables indicating the presence of a muon and an

electron, respectively, in the rest of the event. We consider lepton candidates in the c.m. momentum ranges $1.0 < p_\mu < 2.6 \text{ GeV}/c$ and $0.8 < p_e < 2.6 \text{ GeV}/c$ where the contribution of leptons from semileptonic B decays is enhanced. We require that the leptons are well identified with a likelihood ratio above 0.9. The efficiencies of this requirement are 90% and 87% for muons and electrons, respectively; the probabilities to misidentify hadrons as leptons are at the level of 5%.

For training, we use a simulated $\Upsilon(4S)$ sample that corresponds to an integrated luminosity of 100 fb^{-1} . The training is performed separately for each final-state particle species and for each decay of the unstable particles. The training result, the classifier output, is the probability that a given candidate is a signal. In addition to the variables listed above, the training for each decay also uses the signal probabilities of all direct decay-products. To realize this, the training is performed in stages: first only final state particles and K_S^0 are trained, in the next stage π^0 and J/ψ , then D mesons, subsequently D^* , and finally B mesons.

In the case of multiple B^+ (B^0) candidates, we select the one that has the highest signal probability, \mathcal{P}_B . Figure 1 shows the distribution of $\Delta E'$ versus M_{bc} for combined B^+ and B^0 candidates in the $E_{\text{cm}} = 10.75 \text{ GeV}$ data sample. The $\Delta E'$ variable is defined as

$$\Delta E' = \Delta E + M_{bc} - 5.28 \text{ GeV}, \quad (3.1)$$

where the value 5.28 GeV approximates the B meson mass. Clusters of events are clearly

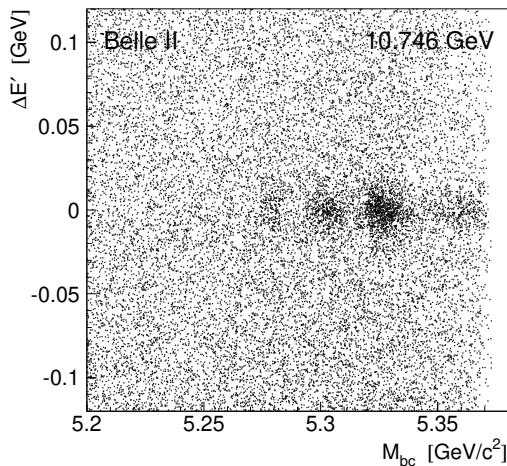


Figure 1: Distributions of $\Delta E'$ vs. M_{bc} in the $E_{\text{cm}} = 10.746 \text{ GeV}$ data sample.

observed at $\Delta E' \approx 0$ with $M_{bc} \approx 5.28, 5.305, \text{ and } 5.33 \text{ GeV}/c^2$, indicating the presence of the $e^+e^- \rightarrow B\bar{B}, B\bar{B}^*, \text{ and } B^*\bar{B}^*$ processes, respectively.

4 Simulation studies and corrections

4.1 Calibration of simulation

Not all channels used for B -meson reconstruction are well measured. Therefore, not all relative yields agree between data and simulation. We introduce weights for simulated events to mitigate this problem.

To determine the weights, we use the $\Delta E'$ distributions in the $\Upsilon(4S)$ sample. We select B candidates with requirements $\mathcal{P}_B > 0.16$ and $M_{bc} > 5.27 \text{ GeV}/c^2$. We perform a simultaneous fit to the $\Delta E'$ distributions in data and simulation for each B -decay channel. The signal in simulation is described by a sum of two Gaussian functions; the signal in data is described by the same model, with the addition of a weight factor, a shift, and a broadening factor, which are all determined by the fit. The background is described by a second order polynomial. The resulting weights are close to 1.0 for two-body decays, while for some multibody decays they are as low as 0.4.

To determine the average shift and broadening factor, we combine all the channels in both data and simulation; for the latter, we apply the weights determined above. We then perform the fit to the $\Delta E'$ distributions in the combined samples. We find that the shift in $\Delta E'$ is negligibly small, $(0.07 \pm 0.07) \text{ MeV}$, while the scale factor for the width is

$$\phi = 1.086 \pm 0.012. \quad (4.1)$$

4.2 Optimization

To optimize the selection in the \mathcal{P}_B and $\Delta E'$ variables, we use a simulated $E_{\text{cm}} = 10.751 \text{ GeV}$ sample with an effective integrated luminosity of 50 fb^{-1} . We maximize the figure-of-merit $S/\sqrt{S+B}$, where S is the number of properly reconstructed signal candidates, and B is the number of all other candidates satisfying $5.270 < M_{bc} < 5.335 \text{ GeV}/c^2$. The optimization is performed iteratively: we scan the figure-of-merit in one variable, then in the other. The resulting values are $|\Delta E'| < 18 \text{ MeV}$ and $\mathcal{P}_B > 0.16$.

Figure 2 shows the M_{bc} distribution in the simulation at $E_{\text{cm}} = 10.751 \text{ GeV}$ after final selection requirements are applied. The signal-to-background ratio is relatively high, which is also the case at the other scan energies. Also shown are the contributions of the continuum and $b\bar{b}$ backgrounds. Candidates in the $b\bar{b}$ samples that do not correspond to generated signal events are treated as background. The continuum background, and in particular $c\bar{c}$, dominates.

4.3 Dependence of the FEI efficiency on E_{cm}

We determine the FEI efficiency as a function of c.m. energy using simulation at the $\Upsilon(4S)$ and scan energies; the results are shown in Fig. 3. The efficiency increases slightly with energy. A fit to a linear function gives the following result:

$$\varepsilon = [(0.6147 \pm 0.0007) + (0.068 \pm 0.026) \text{ GeV}^{-1} \times (E_{\text{cm}} - 10.5796 \text{ GeV})] \times 10^{-3}. \quad (4.2)$$

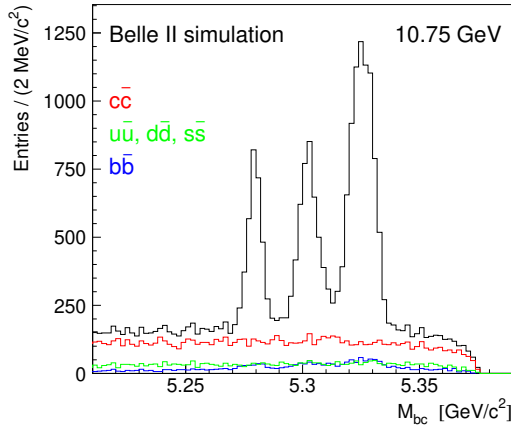


Figure 2: Distribution of M_{bc} in simulation at $E_{\text{cm}} = 10.751$ GeV. The background contributions are also shown: $c\bar{c}$ (red), the sum of $u\bar{u}$, $d\bar{d}$, and $s\bar{s}$ (green), and $b\bar{b}$ (blue).

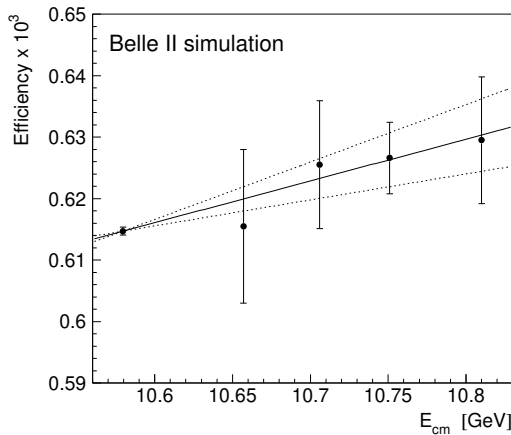


Figure 3: Reconstruction efficiency of the FEI at various c.m. energies determined using simulation. The solid line is the result of the fit to a linear function, and the dashed lines show the results when the slope parameter is varied by ± 1 standard deviation.

Here, 10.5796 GeV is the simulated $\Upsilon(4S)$ energy. The above fit result corresponds to a 1.032 ± 0.012 ratio between efficiencies at the $\Upsilon(5S)$ energy (10.866 GeV) and at the $\Upsilon(4S)$ energy. This value agrees with the Belle measurement performed using $\Upsilon(4S)$ and $\Upsilon(5S)$ data, 1.049 ± 0.032 [8].

5 Absolute value of the FEI efficiency

To determine the absolute value of the FEI efficiency we use the $\Upsilon(4S)$ data. The efficiency is calculated as

$$\varepsilon = N / (2 N_{B\bar{B}}), \quad (5.1)$$

where N is the number of reconstructed B mesons using the FEI and $N_{B\bar{B}}$ is the total number of $B\bar{B}$ events determined by counting hadronic events and subtracting the continuum contribution: $N_{B\bar{B}} = (38.67 \pm 0.58) \times 10^6$.

The B -meson yield N is determined using a fit to the M_{bc} distribution. We use the fit function that was developed in Ref. [8]. It is calculated numerically as a sequence of convolutions and includes the effects of the energy spread of the colliding beams, initial-state radiation (ISR), the B -meson momentum resolution, and the energy dependence of the production cross-section. The latter plays an important role if the cross section changes noticeably over the typical range of the E_{cm} spread, which is the case at the $\Upsilon(4S)$. In Sections 5.1 and 5.2, we describe, respectively, the determination of the momentum resolution function, and the study of background and broken signal distributions in simulation. We then present the fit to the $\Upsilon(4S)$ data, estimate systematic uncertainties on its results, and calculate the FEI efficiency (Sections 5.3 to 5.4).

5.1 Momentum resolution

At the $\Upsilon(4S)$ energy, the resolution in M_{bc} is dominated by the E_{cm} spread. The B -momentum resolution plays a minor role because it contributes proportionally to the B momentum, which is small at the $\Upsilon(4S)$ resonance. However, the effect of the momentum resolution becomes prominent at scan energies. Thus, we take it into account consistently for all data samples.

The momentum resolution is parameterized as

$$f(p - p_0) = \frac{1 - r_2 - r_3}{\sigma_1} \exp\left[-\frac{(p - p_0 - \mu_1)^2}{2\sigma_1^2}\right] p \left\{ 1 - \exp\left[-\frac{2p(p_0 + \mu_1)}{\sigma_1^2}\right] \right\} \\ + \frac{r_2}{\sigma_2} \exp\left[-\frac{(p - p_0 - \mu_2)^2}{2\sigma_2^2}\right] p \left\{ 1 - \exp\left[-\frac{2p(p_0 + \mu_2)}{\sigma_2^2}\right] \right\} \\ + \frac{r_3}{\sigma_3} \exp\left[-\frac{(p - p_0 - \mu_3)^2}{2\sigma_3^2}\right] p \left\{ 1 - \exp\left[-\frac{2p(p_0 + \mu_3)}{\sigma_3^2}\right] \right\}, \quad (5.2)$$

where p and p_0 are the reconstructed and true B -meson momenta, respectively. This function is a sum of three Gaussians with parameters μ_i and σ_i , and weights r_i , each multiplied by an additional factor. The extra factor takes into account the fact that p is positive definite, and is obtained by considering the momentum-resolution function in three dimensions and analytically integrating out all variables other than p . To determine the parameters of the resolution function, we fit the $p - p_0$ distribution in the simulated $\Upsilon(4S)$ sample; the results are presented in Table 2 (f_A column).

5.2 Backgrounds and broken signal

Figure 4 shows the M_{bc} distributions for three categories of candidates in the $\Upsilon(4S)$ simulation: (1) truth matched (correctly reconstructed B mesons), (2) non-truth matched, and (3) candidates in the $\Delta E'$ sideband. The $\Delta E'$ sideband has the same width as the signal region, while its center is shifted by +80 MeV. There is a peaking structure in the distributions of non-truth matched candidates and candidates in the $\Delta E'$ sideband. This structure is due to signal decays in which one of the final state particles is swapped with a background particle. The magnitude of this broken signal component is proportional to the signal yield, while its M_{bc} distribution is broader due to the incorrectly reconstructed

Table 2: Parameters of the momentum resolution functions of Eq. (5.2) for truth-matched candidates (f_A) and unmatched candidates in the $\Delta E'$ signal region (f_B) and sideband (f_C). The parameters w are the relative weights of the three peaking components.

	f_A	f_B	f_C
w	1	0.048	0.0149
μ_1 (MeV/ c)	-0.02	0.7	-21
σ_1 (MeV/ c)	4.4	14	115
r_2	0.48	0.48	0
μ_2 (MeV/ c)	-0.02	-15	-
σ_2 (MeV/ c)	8.0	95	-
r_3	0.082	0	0
μ_3 (MeV/ c)	0.03	-	-
σ_3 (MeV/ c)	17.1	-	-

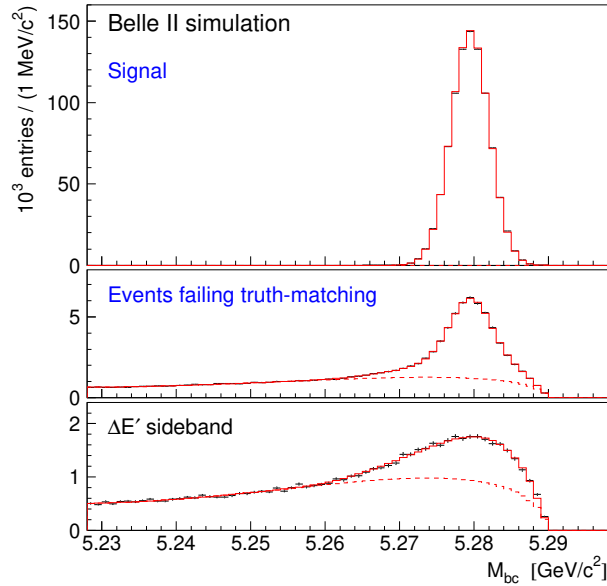


Figure 4: Distributions of M_{bc} for the simulated $\Upsilon(4S)$ sample. The top and middle panels show truth-matched and non-truth matched candidates, respectively, while the bottom panel shows candidates in the $\Delta E'$ sideband. The solid histogram shows the result of the simultaneous fit, and the dashed histogram shows the distribution of background events.

momentum of the decay products. Thus, it can be described by a M_{bc} signal function with a poor momentum resolution.

To determine the ratio of the broken signal yield to that of the signal (w) and the parameters of the momentum-resolution function describing the broken signal, we perform a simultaneous fit to the three M_{bc} distributions shown in Fig. 4. For the truth-matched component, the parameters of the momentum resolution function are fixed to the values obtained using the momentum-difference fit described in the previous section. For the broken signal components, the parameters of the resolution function are left free. The simulation does not include the ISR process; we modify the M_{bc} signal function accordingly. The production cross-section is energy-independent in the simulation.

The smooth background is described by a square-root function multiplied by a third-order Chebyshev polynomial. The parameters of the polynomial are all determined by the fit. The shape of the smooth background is the same in the $\Delta E'$ signal region and in the sideband, while the normalizations are independent. The fits to M_{bc} distributions in this paper are binned likelihood fits.

The fit results are shown in Table 2 (columns f_B and f_C for the broken signal components in the $\Delta E'$ signal region and sideband, respectively). In the $\Delta E'$ signal region, two Gaussian functions are sufficient, while in the sideband, one Gaussian function is sufficient.

5.3 Fit to the $\Upsilon(4S)$ data

To determine the B -meson yield in the $\Upsilon(4S)$ data sample and to find corrections to the model of the broken signal component, we fit the M_{bc} distribution in $\Upsilon(4S)$ data. In addition to the steps discussed in the previous section, this requires the inclusion of ISR and the energy dependence of the cross section. Below the $B\bar{B}^*$ threshold, the $e^+e^- \rightarrow B\bar{B}$ cross section coincides with the total $b\bar{b}$ cross section, usually presented in terms of R_b

$$R_b = \frac{\sigma(b\bar{b})}{\sigma_0(\mu^+\mu^-)}, \quad (5.3)$$

where $\sigma_0(\mu^+\mu^-)$ is the Born cross section for $e^+e^- \rightarrow \mu^+\mu^-$. We use the most precise measurement of the energy dependence of R_b from Ref. [26]. Since no suitable physics-motivated model of the R_b shape is available, we use an 11th order Chebyshev polynomial, as in Ref. [8]. We parameterize the dressed cross section² and apply the ISR correction and the energy-spread correction by performing convolutions with the ISR radiation kernel [25] and a Gaussian function with the standard deviation fixed to the BaBar energy spread, respectively.

The R_b -shape measurement [26] is insufficiently precise to use as a simple input to this procedure: not all curves that give acceptable fit quality to the R_b scan also satisfactorily describe the M_{bc} distribution. Therefore, we perform a simultaneous fit to the energy dependence of R_b and the M_{bc} distributions in the $\Delta E'$ signal and sideband regions. The inclusion of the $\Delta E'$ sideband in the fit helps to constrain the smooth background and to find corrections for the yield and shape of the broken signal component.

²The difference between the dressed and Born cross sections is that the former takes into account the vacuum polarization effect.

The R_b points have a sizeable energy scale uncertainty of 1.5 MeV [26]. Hence, in Ref. [8] Belle introduced a common shift in the c.m. energy of all the R_b scan points, and determined the value $\Delta E_{\text{BaBar}} = (-1.75 \pm 0.68) \text{ MeV}$ from the fit. We introduce the ΔE_{BaBar} shift and fix its value to the Belle result.

Simulation shows that the scale factor of the momentum resolution is approximately the same as that of the $\Delta E'$ signal. Therefore, all the width parameters of the f_A component of the resolution function are multiplied by the scale factor of Eq. (4.1). The same scale factor is applied to the narrow Gaussian in the function f_B describing the broken signal in the $\Delta E'$ signal region. For the function f_C describing the broken signal in the $\Delta E'$ sideband, we introduce a normalization correction n_3 , shift s_3 , and width scale factor ϕ_3 . All these parameters are free in the fit. Unlike the Belle analysis [8], we do not use a low $\Delta E'$ sideband, as it was found to contain a tail of the signal and a small contribution from Cabibbo-suppressed decays, such as DK and $DK\pi\pi$, with the kaon misidentified as a pion. The high $\Delta E'$ sideband provides more accurate information about the broken signal component. The smooth background is parameterized as described in the previous section for simulation.

The fit results are presented in Figs 5 and 6, and in Table 3.

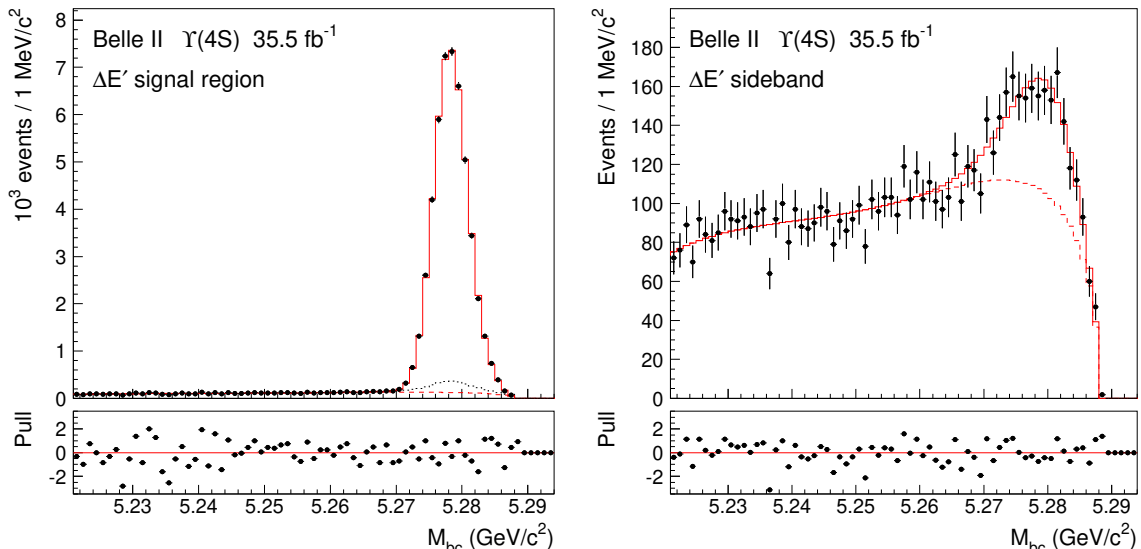


Figure 5: Distributions of M_{bc} for $\Upsilon(4S)$ data. The left and right panels correspond to the $\Delta E'$ signal and sideband regions. The solid histogram shows the result of the simultaneous fit to these distributions and the cross-section energy dependence (Fig. 6). The red dashed histogram shows the background, and the black dotted histogram shows the sum of the background and the broken signal (in the right panel, this coincides with the total fit, and is thus not visible). The bottom panels show pulls (deviations of the data points from the fit function divided by the uncertainties on the data).

5.3.1 Systematic uncertainties at the $\Upsilon(4S)$

We study systematic uncertainties from various sources (Table 4).

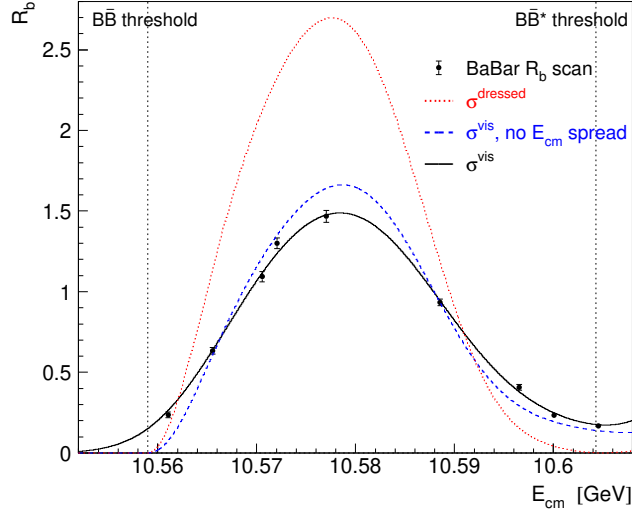


Figure 6: Energy dependence of the total $b\bar{b}$ cross section (R_b). Points with error bars are from Ref. [26]. The black solid curve is the result of the simultaneous fit to this distribution and the M_{bc} distributions (Fig. 5). The blue dashed curve is the visible cross section before accounting for the E_{cm} spread. The red dotted curve is the dressed cross section. The vertical dotted lines indicate the $B\bar{B}$ and $B\bar{B}^*$ thresholds.

Table 3: Results of the simultaneous fit to the M_{bc} distributions in the $\Upsilon(4S)$ data and the R_b scan results of BaBar [26]. The lower three parameters are explained in the text. The first uncertainty is statistical, the second one (if present) is systematic.

Signal yield	$(45.57 \pm 0.24 \pm 0.16) \times 10^3$
Nominal E_{cm}	$(10579.80 \pm 0.12 \pm 0.78) \text{ MeV}$
E_{cm} spread	$(5.62 \pm 0.19 \pm 0.27) \text{ MeV}$
n_3	$1.03^{+0.20}_{-0.23}$
s_3	$(7.5^{+11.1}_{-8.8}) \text{ MeV}/c$
ϕ_3	$0.630^{+0.107}_{-0.101}$

- We vary the B^+ and B^0 masses within their uncertainties. We use the Particle Data Group average values $m(B^+) = (5279.25 \pm 0.26) \text{ MeV}/c^2$ and $m(B^0) = (5279.63 \pm 0.20) \text{ MeV}/c^2$ [27] instead of their fit values because the latter include the measurement of $m(B^0) - m(B^+)$ at the $\Upsilon(4S)$, performed by BaBar [28], that overlooks a source of systematic bias according to Ref. [29].
- We use the cross section shape measured by Belle [8]. We find that $-2 \ln \mathcal{L}$ increases by 11.0, which, for a model with 11 fewer parameters, corresponds to an exclusion level of 0.8σ . Thus, the two shapes agree well.
- We vary the ΔE_{BaBar} shift by one standard deviation from Ref. [8].

- In the default fit, the corrections are applied only to the broken signal component in the sideband. We apply the corrections also to the broad broken signal component in the signal region assuming them to be the same.
- The uncertainty due to the scale factor of Eq. (4.1) is found to be negligibly small.

In each case, the largest variation is taken as the uncertainty. The total systematic uncertainty is obtained by summing the individual contributions in quadrature.

Table 4: Systematic uncertainty in the B -meson yield at the $\Upsilon(4S)$, nominal E_{cm} (in MeV), and E_{cm} spread (in MeV).

	$N, 10^3$	E_{cm}	Spread
B^+ mass	0.01	0.47	0.04
B^0 mass	0.01	0.32	0.09
Cross section shape	0.05	0.10	0.02
Energy scale of the BaBar scan data	0.03	0.53	0.25
Treatment of broken signal	0.15	0.02	0.00
Total	0.16	0.78	0.27

5.4 Determination of the FEI efficiency at the $\Upsilon(4S)$

We determine the absolute value of the FEI efficiency at the $\Upsilon(4S)$ using (5.1) to be

$$\varepsilon = (0.5892 \pm 0.0031 \pm 0.0116) \times 10^{-3}, \quad (5.4)$$

where the first uncertainty is statistical and the second is systematic. The efficiency is higher than that at Belle, 0.469×10^{-3} [8], possibly due to Belle II's higher reconstruction efficiency for low-momentum charged particles. The efficiency values at various energies determined from simulation (Eq. (4.2)) are multiplied by a correction factor 0.959 ± 0.020 which is the ratio of the value in Eq. (5.4) and the constant term in Eq. (4.2).

We consider contributions of the systematic uncertainties in N (0.3%) and $N_{B\bar{B}}$ (1.5%). To check the stability of the efficiency over the running period, we subdivide the $\Upsilon(4S)$ sample into three parts (one before the energy scan and two after) and determine the efficiency in each. Based on the dispersion of these measurements, we assign an additional 1.2% systematic uncertainty due to long-term variations. The total relative uncertainty in the FEI efficiency, obtained by adding the statistical and systematic contributions in quadrature (Eq. (5.4)), is 2.0%.

6 Measurements at the scan energies

To determine the signal yields at various energies, we perform the M_{bc} fits as described in Section 6.1. The energy dependence of the $e^+e^- \rightarrow B\bar{B}$, $B\bar{B}^*$, and $B^*\bar{B}^*$ cross sections

influences the corresponding peak positions (due to the finite energy spread [29]) and ISR tails. Thus, energy-dependence information is needed to determine the signal function in the M_{bc} fit. The fit to the energy dependence is described in Section 6.2. To obtain self-consistent results, we use an iterative procedure: (1) we fit the M_{bc} spectra; (2) based on the signal yields, we determine the cross sections; and (3) we fit the energy dependence of the cross sections. We use the cross-section shapes measured by Belle as a starting point [8]. Two iterations are sufficient for convergence. We report on the study of systematic uncertainties in Section 6.3.

6.1 M_{bc} fits at scan energies

To fit the M_{bc} distributions at the scan energies, we also include the $e^+e^- \rightarrow B\bar{B}^*$ and $e^+e^- \rightarrow B^*\bar{B}^*$ components. Decays $B^* \rightarrow B\gamma$ lead to additional smearing of the B momentum, which is accounted for in the fit function [8]. The resulting M_{bc} distribution is sensitive to the distribution in the B^* helicity angle, which is the angle between the B momentum in the B^* rest frame and the B^* boost direction. For the $e^+e^- \rightarrow B\bar{B}^*$ process, the helicity-angle distribution is fixed by conservation laws: $1 + \cos^2 \theta_h$. For the $e^+e^- \rightarrow B^*\bar{B}^*$ process, the distribution depends on an unknown parameter a_h : $1 + a_h \cos^2 \theta_h$, with $-1 \leq a_h \leq 1$; the parameter a_h is left free in the fits.

The E_{cm} value and the E_{cm} spread are determined by the fit for all scan data samples. The resolution-function parameters and the broken-signal corrections (n_3 , s_3 , and ϕ_3) are taken to be the same as in the $\Upsilon(4S)$ data (Tables 2 and 3).

The fit interval is from $5.2 \text{ GeV}/c^2$ up to the kinematic boundary at $E_{cm}/2$. The smooth background is described by a square-root function multiplied by a Chebyshev polynomial; we use third order for the two higher scan energies and second order for the two lower ones. (A larger fit interval requires a higher polynomial order; we find that increasing the polynomial orders further does not significantly improve the $-2 \ln \mathcal{L}$ of the fit.)

Fit results for the scan data are shown in Fig. 7, and Tables 5 and 6. The $B\bar{B}$

Table 5: Yields of the $e^+e^- \rightarrow B\bar{B}$, $B\bar{B}^*$, and $B^*\bar{B}^*$ processes in the scan data samples. The uncertainties are statistical.

point#	$B\bar{B}$	$B\bar{B}^*$	$B^*\bar{B}^*$
1	90.1 ± 17.5	401.7 ± 27.9	525.4 ± 30.8
2	174.5 ± 26.7	535.6 ± 42.6	931.5 ± 42.7
3	21.8 ± 8.2	189.9 ± 17.8	202.5 ± 17.9
4	32.2 ± 14.6	321.5 ± 23.5	151.4 ± 15.0

component has a peak near the kinematic boundary, which is due to the ISR production of $\Upsilon(4S)$ followed by decay to $B\bar{B}$. The contribution of this process is fixed in the fits to the value calculated using the energy dependence of the $e^+e^- \rightarrow B\bar{B}$ dressed cross-section between the $B\bar{B}$ and $B\bar{B}^*$ thresholds, the reconstruction efficiency, and the luminosity of each scan data sample. The data do not show any excess due to the three-body processes

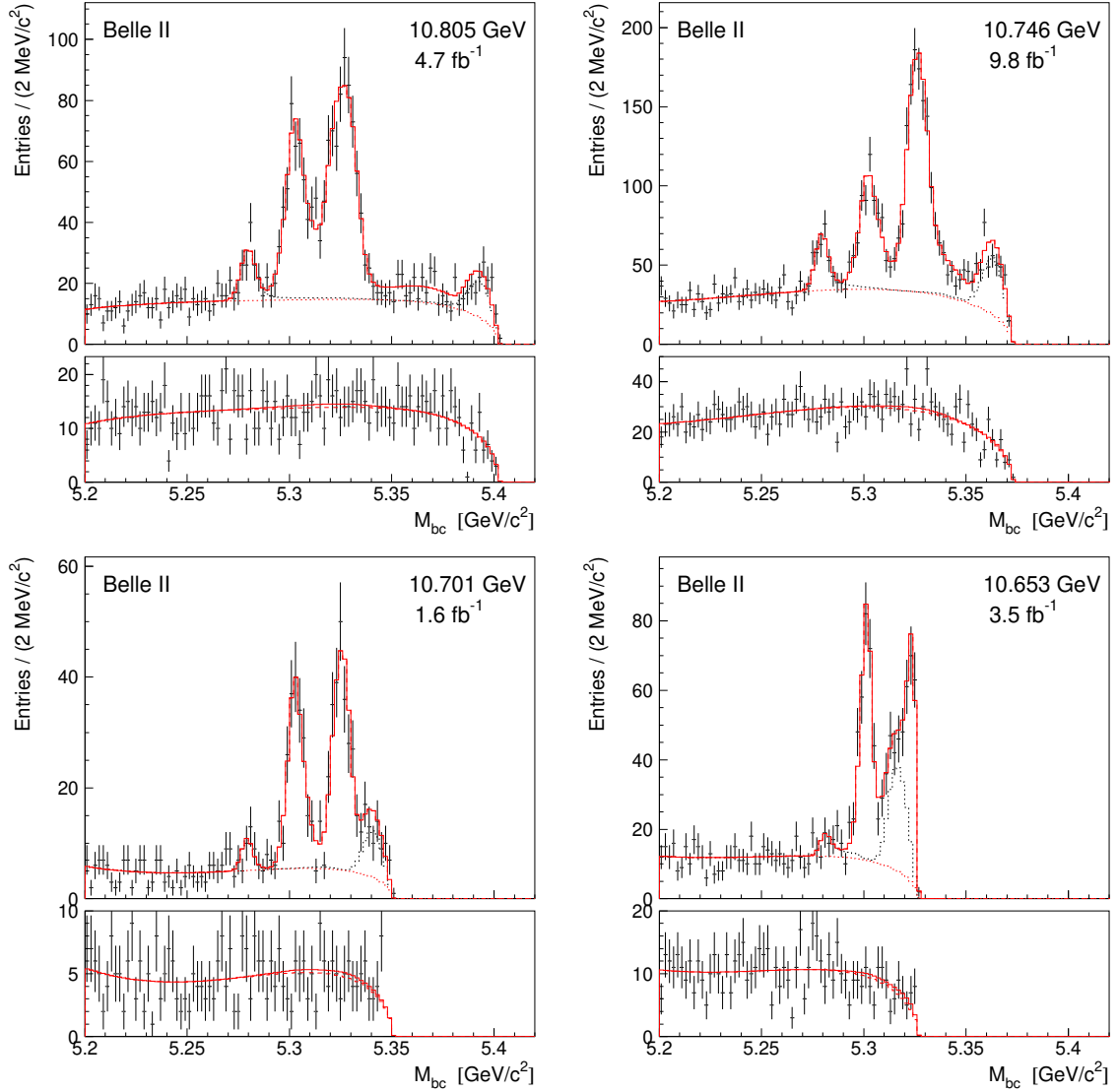


Figure 7: Distributions of M_{bc} for the four scan energies. In each figure the top panel corresponds to the $\Delta E'$ signal region, and the bottom to the sideband. The red solid histogram shows the result of the fit; the red dashed histogram shows the smooth background; and the black dotted histogram shows the sum of the smooth background and the $B\bar{B}$ channel, which includes a peak near the threshold due to the ISR production of $\Upsilon(4S)$.

$e^+e^- \rightarrow B^{(*)}\bar{B}^{(*)}\pi$, whose signals are situated near the M_{bc} kinematic boundary and have shapes similar to that of the ISR production of $\Upsilon(4S)$. The absence of $B^{(*)}\bar{B}^{(*)}\pi$ signals is consistent with the observation that two-body processes $B^{(*)}\bar{B}^{(*)}$ saturate the total $b\bar{b}$ cross section below an energy of about 10.81 GeV (see Fig. 14 below). The yields are defined as the integrals of the signal components up to $M_{bc} = 5.35 \text{ GeV}/c^2$. At the two lowest scan energies, ISR production of the $\Upsilon(4S)$ starts to contribute to the above interval; the corresponding events are excluded from the signal yield of $e^+e^- \rightarrow B\bar{B}$.

Table 6: Results for the energy and energy spread of the scan data samples. The first uncertainty is statistical, the second is uncorrelated systematic, and the third is correlated systematic.

point#	E_{cm} (MeV)	E_{cm} spread (MeV)
1	$10804.50 \pm 0.65 \pm 0.25 \pm 0.50$	$6.44 \pm 0.85 \pm 0.16 \pm 0.13$
2	$10746.30 \pm 0.46 \pm 0.15 \pm 0.50$	$5.68 \pm 0.69 \pm 0.29 \pm 0.09$
3	$10700.90 \pm 0.61 \pm 0.14 \pm 0.50$	$4.85 \pm 0.95 \pm 0.14 \pm 0.05$
4	$10653.30 \pm 0.71 \pm 0.89 \pm 0.50$	$5.23 \pm 0.57 \pm 0.66 \pm 0.20$

The measured E_{cm} values agree with the results of the $e^+e^- \rightarrow \mu^+\mu^-$ analysis; the difference between the two measurements, $E_{\text{cm}}(B) - E_{\text{cm}}(\mu^+\mu^-)$, is shown in Fig. 8 (left). The E_{cm} spread values (Fig. 8 (right)) are consistent across the scan data samples and

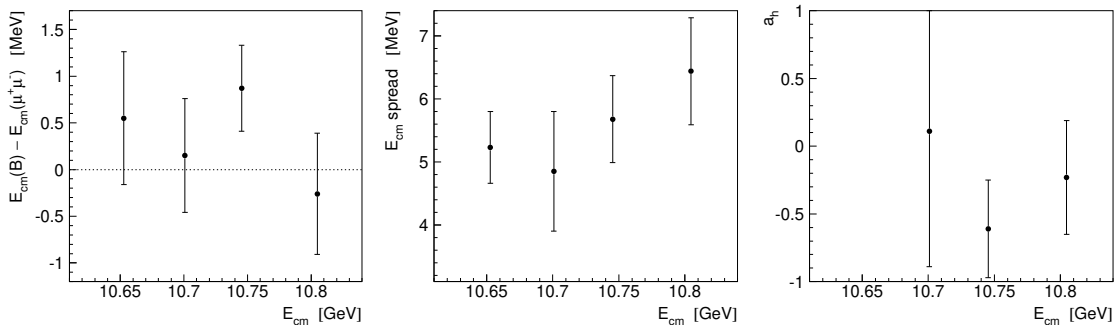


Figure 8: Measurements of $E_{\text{cm}}(B) - E_{\text{cm}}(\mu^+\mu^-)$ (left), E_{cm} spread (middle), and helicity parameter a_h (right) at various energies. Error bars show statistical uncertainties. The uncorrelated and correlated uncertainties of $E_{\text{cm}}(\mu^+\mu^-)$ are at the level of 0.3 MeV and 1 MeV, respectively, and are not included.

agree with the $\Upsilon(4S)$ measurement (Table 3). The results for the helicity parameter a_h (Fig. 8 (right)) are also consistent among the scan data samples and agree with the value -0.18 ± 0.07 measured by Belle at the $\Upsilon(5S)$ energy [8]. As E_{cm} decreases, the $B^*\bar{B}^*$ signal width becomes smaller and sensitivity to a_h drops. At the lowest E_{cm} we set $a_h = 0$; variations $a_h = -1$ and $a_h = +1$ produce negligible changes in the yields.

We calculate the dressed cross sections as

$$\sigma^{\text{dressed}} = \frac{N}{(1 + \delta_{\text{ISR}}) L \varepsilon}, \quad (6.1)$$

where N is the signal yield; $(1 + \delta_{\text{ISR}})$ is the radiative correction, calculated based on the cross-section shapes (Fig. 9 below) as described in Section 5.3; L is the integrated luminosity; and ε is the reconstruction efficiency. The $(1 + \delta_{\text{ISR}})$ values are shown in Table 7. Results for the $e^+e^- \rightarrow B\bar{B}$, $e^+e^- \rightarrow B\bar{B}^*$, and $e^+e^- \rightarrow B^*\bar{B}^*$ processes are presented in Table 8 and Fig. 9. The cross sections match well with the previous measurement by Belle [8] and have better precision.

Table 7: Values of $(1 + \delta_{\text{ISR}})$ calculated using the cross-section shapes shown in Fig. 9.

point#	$B\bar{B}$	$B\bar{B}^*$	$B^*\bar{B}^*$
1	0.757	0.719	0.646
2	0.781	0.860	0.760
3	0.696	0.773	0.686
4	1.063	0.720	0.561

Table 8: Results for the $e^+e^- \rightarrow B\bar{B}$, $B\bar{B}^*$, and $B^*\bar{B}^*$ cross sections. The first uncertainty is statistical, the second is uncorrelated systematic and the third is correlated systematic.

point#	$\sigma(e^+e^- \rightarrow B\bar{B})$ (pb)	$\sigma(e^+e^- \rightarrow B\bar{B}^*)$ (pb)	$\sigma(e^+e^- \rightarrow B^*\bar{B}^*)$ (pb)
1	$21.0 \pm 4.1 \pm 0.5 \pm 0.5$	$98.6 \pm 6.8 \pm 1.3 \pm 2.3$	$143.6 \pm 8.4 \pm 2.4 \pm 3.3$
2	$19.0 \pm 2.9 \pm 1.0 \pm 0.4$	$52.9 \pm 4.2 \pm 1.0 \pm 1.2$	$104.0 \pm 4.8 \pm 2.7 \pm 2.4$
3	$16.1 \pm 6.0 \pm 0.7 \pm 0.4$	$126.0 \pm 11.8 \pm 2.2 \pm 2.8$	$151.4 \pm 13.4 \pm 2.8 \pm 3.4$
4	$7.2 \pm 3.3 \pm 1.4 \pm 0.2$	$106.8 \pm 7.8 \pm 3.7 \pm 2.3$	$64.5 \pm 6.4 \pm 2.7 \pm 1.4$

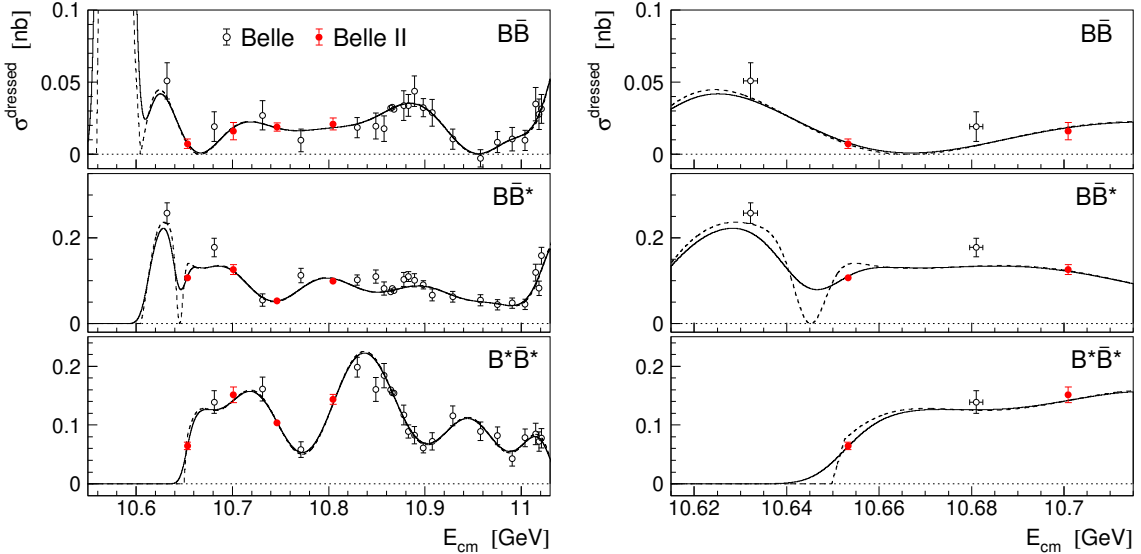


Figure 9: Energy dependence of the $e^+e^- \rightarrow B\bar{B}$ (top), $B\bar{B}^*$ (middle), and $B^*\bar{B}^*$ (bottom) cross sections. Red circles show the Belle II results obtained in this analysis; the error bars indicate the statistical uncertainty. The black open circles show the Belle measurements from Ref. [8]; the error bars show combined statistical and uncorrelated systematic uncertainties. The solid curves show the result of the fit to these three distributions and to the total $b\bar{b}$ cross section shown in Fig. 10. The dashed curves show the fit function before the convolution accounting for the E_{cm} spread. Plots on the left show the full fit range; on the right, the $B^*\bar{B}^*$ threshold region is magnified.

6.2 Fit to the energy dependence of the cross sections

We perform a simultaneous fit to the energy dependence of the exclusive $e^+e^- \rightarrow B\bar{B}$, $e^+e^- \rightarrow B\bar{B}^*$, and $e^+e^- \rightarrow B^*\bar{B}^*$ cross sections, and the total $e^+e^- \rightarrow b\bar{b}$ cross section. For the exclusive cross sections, we use both the Belle II results and the Belle measurements from Ref. [8]. For the total cross section, we use the data from Ref. [7], where the BaBar and Belle energy scan results [26, 31] are combined and radiative corrections are applied to convert the visible cross section into the dressed one. The total cross section shows deep minima or zeros at the $B\bar{B}^*$ and $B^*\bar{B}^*$ thresholds (Fig. 10). These structures motivate inclusion of the total cross section in the fit. The total cross section is fitted only up to 10.75 GeV (the $B\bar{B}^*\pi$ threshold); its fit function is the sum of the fit functions of the exclusive channels. The $\Upsilon(4S)$ peak region, where the dressed cross section reaches approximately 2 nb, is shown in more detail in Fig. 14 below.

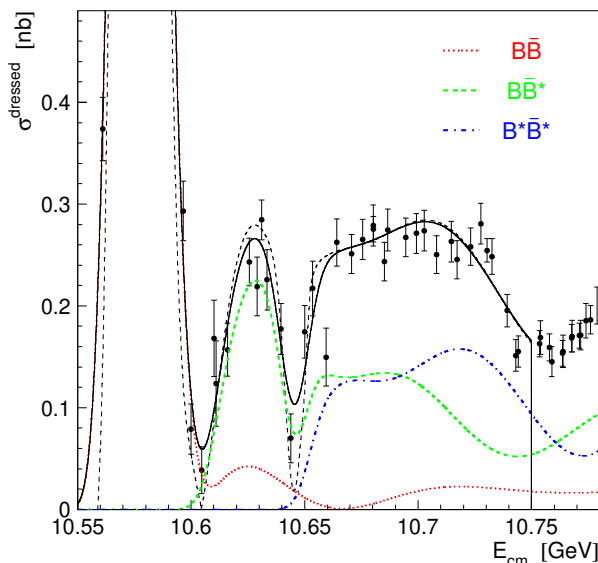


Figure 10: Energy dependence of the total $b\bar{b}$ dressed cross section from Ref. [7] (circles). The solid black curve shows the result of the simultaneous fit to this distribution and the exclusive $B\bar{B}$, $B\bar{B}^*$, and $B^*\bar{B}^*$ cross section energy dependence (Fig. 9). The vertical line at 10.75 GeV indicates the upper boundary of the fit interval. The dashed black curve shows the fit function before the convolution accounting for the E_{cm} spread. Also shown are the individual contributions of $B\bar{B}$ (red dotted), $B\bar{B}^*$ (green dashed), and $B^*\bar{B}^*$ (blue dash-dotted).

To fit the $e^+e^- \rightarrow B\bar{B}$ cross section we use a 13th order Chebyshev polynomial. Since there is a zero at the $B\bar{B}^*$ threshold ($E_{B\bar{B}^*} = 10604.3 \text{ MeV}$) in the fit shown in Fig. 6, the cross section is fitted only above the $B\bar{B}^*$ threshold. We impose the requirement that the polynomial is zero at the $B\bar{B}^*$ threshold by adding a point there with zero cross section and a small uncertainty. Below the $B\bar{B}^*$ threshold, we use the cross-section shape obtained in the analysis of the $\Upsilon(4S)$ data (Fig. 6).

To fit the $e^+e^- \rightarrow B\bar{B}^*$ cross section we use a 14th order Chebyshev polynomial

plus a Gaussian $A_0 \exp\{-(x - E_0)^2/2\sigma_0^2\}$ to describe the dip at the $B^*\bar{B}^*$ threshold ($E_{B^*\bar{B}^*} = 10649.7 \text{ MeV}$). We impose a requirement that the polynomial is equal to zero at the $B\bar{B}^*$ threshold. The parameters of the Gaussian are free in the fit. We find $A_0 = (-0.180_{-0.018}^{+0.039}) \text{ nb}$, $E_0 = (10644.9_{-1.4}^{+1.2}) \text{ MeV}$, and $\sigma_0 = (3.5_{-0.5}^{+1.4}) \text{ MeV}$.

The shape of the $e^+e^- \rightarrow B^*\bar{B}^*$ cross section is parameterized using a 13th order Chebyshev polynomial and a linear function at the threshold. The data in Figs. 9 and 10 show that the $e^+e^- \rightarrow B^*\bar{B}^*$ cross section increases rapidly above the $B^*\bar{B}^*$ threshold. To describe this increase, we use the function

$$f_1(E_{\text{cm}}) = \frac{1}{k} (E_{\text{cm}} - E_{B^*\bar{B}^*}). \quad (6.2)$$

We do not impose a requirement of a zero for the high-order polynomial, and the fit function is equal to whichever is smaller: $f_1(E_{\text{cm}})$ or the high-order polynomial. The fit to the energy dependence of the cross sections is not sensitive to the slope of $f_1(E_{\text{cm}})$. However, the shape of the M_{bc} distribution at the energy $E_{\text{cm}} = 10653.3 \text{ MeV}$ (only about 4 MeV above the $B^*\bar{B}^*$ threshold) is sensitive to the slope. The parameter k is free in the corresponding fit (Fig. 7 (bottom right)) and equals $k = (37 \pm 13) \text{ MeV/nb}$. This shows that the $B^*\bar{B}^*$ cross section reaches the typical level of 0.1 nb within 3.7 MeV from the threshold. Thus, the shape of the M_{bc} distribution provides further support for the rapid rise of the $B^*\bar{B}^*$ cross section.

The degrees of the polynomials chosen are the lowest that provide reasonable descriptions of the shape, while also allowing for variations in degree to estimate systematic uncertainties.

6.3 Systematic uncertainties

We consider the following sources of uncorrelated systematic uncertainty:

- Cross section shape — model: we change the orders of the Chebyshev polynomials used to parameterize the cross section shapes by ± 1 , $+2$, and $+3$ in all three channels simultaneously. We repeat the M_{bc} fits using the new cross-section shapes and take the root-mean-square (RMS) deviation of the measured quantities as the uncertainty. These are small compared to the statistical uncertainties.
- Cross section shape — uncertainty in measurements: we use pseudoexperiments generated using the fitted values of the cross sections and the uncertainties found in data. The Belle measurements of the exclusive cross sections and the measurements of the total cross section are also varied. For each pseudoexperiment, we fit the energy dependence of the cross sections and perform the M_{bc} fits using the resulting cross-section shapes. The RMS deviation of the measured quantities is taken as the uncertainty. This source is found to give the largest contribution; however, it is small compared to the statistical uncertainties. Figure 11 shows examples of fits to the pseudoexperiments and the systematic uncertainties from this source.
- Broken signal: we consider the same variation of the fit as described above for the $\Upsilon(4S)$ analysis (Section 5.3.1). Namely, in the default fit the corrections are applied

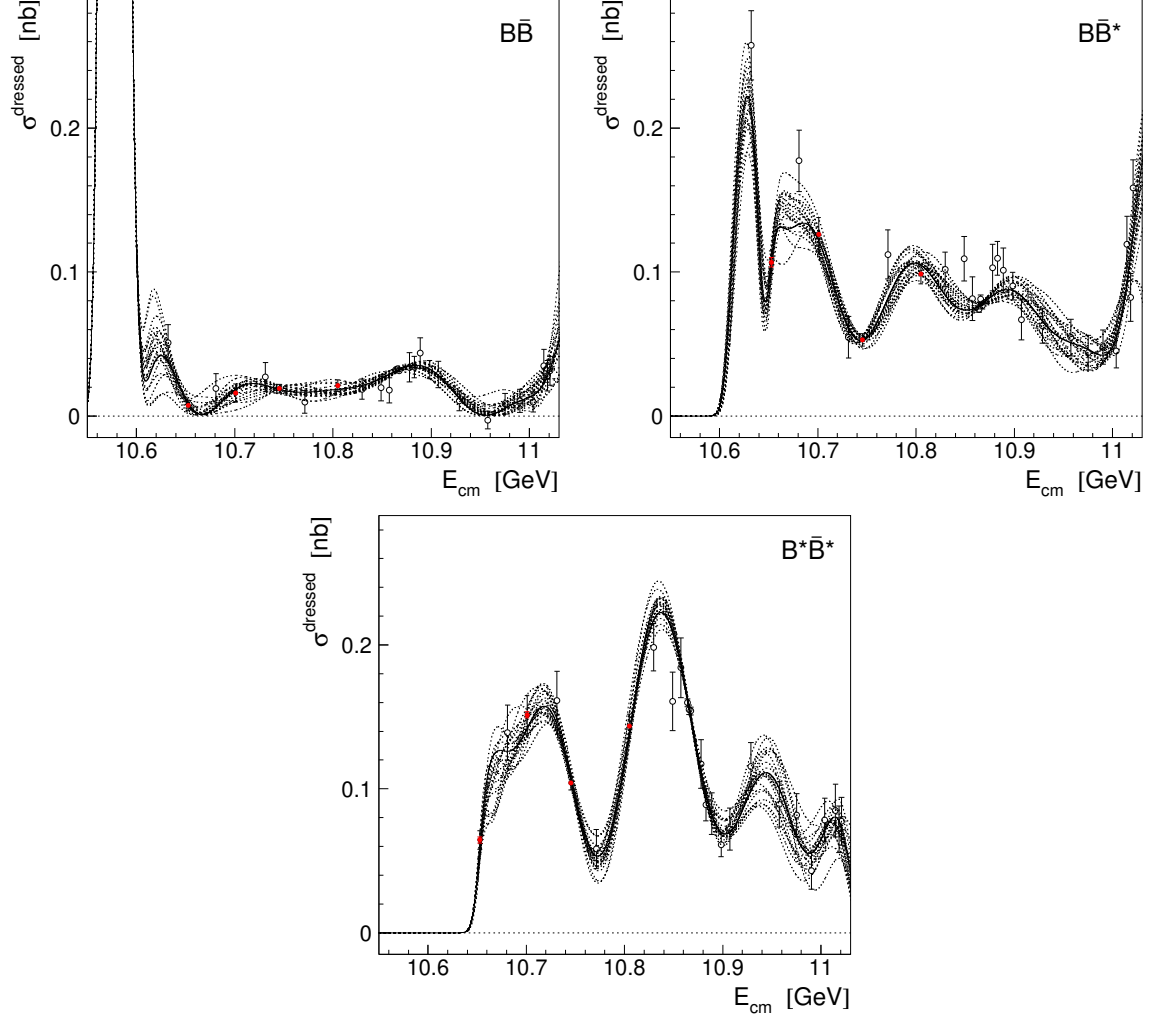


Figure 11: Energy dependence of the $e^+e^- \rightarrow B\bar{B}$ (left), $B\bar{B}^*$ (right), and $B^*\bar{B}^*$ (bottom) cross sections. Red filled and black open circles show the Belle II and Belle measurements, respectively. In the Belle II results, black error bars show statistical uncertainties and red error bars show systematic uncertainties related to the shape of the cross section energy dependence, estimated using pseudoexperiments. (On nine out of the twelve points, the systematic uncertainties are smaller than the size of the red filled circle, and thus not visible.) The solid curves show the default fit result; the dashed curves show the results of the fits to various pseudoexperiments.

only to the broken signal component in the sideband. We apply the corrections also to the broad broken signal component in the signal region assuming that they are the same as for the broken signal component in the sideband. The uncertainties due to this source are small.

- Shape of the smooth background: in the default fit the smooth background is described by a threshold function multiplied by 2nd or 3rd order Chebyshev polynomial (Section 6.1). We increase the order of the polynomial by one and two units. The uncertainties due to this source are small.

The total uncorrelated systematic uncertainty is obtained by adding the above contributions in quadrature; it is shown in Figs. 12 and 13, and in Tables 6 and 8. For simplicity, in the default fit to the cross section energy dependence, we use only statistical uncertainties of the Belle II measurements. We repeat the fit combining statistical and uncorrelated systematic uncertainties for Belle II and find that the change in the results is negligibly small.

Correlated systematic uncertainty in the cross sections has the following sources:

- Uncertainty in the absolute value of the efficiency of 2.1% determined using the $\Upsilon(4S)$ data (Section 5.4).
- Uncertainty in the energy dependence of the efficiency. For the efficiency, we use the values of the fit function shown in Fig. 3. The uncertainty due to the limited size of the simulated samples has values in the range 0.3% – 0.8%, increasing linearly with E_{cm} .
- Uncertainty in the luminosity of 0.6% [30].

The effect of the uncertainties in the B and B^* masses on the cross sections is negligibly small. The total correlated systematic uncertainties shown in Table 8 are obtained by adding the above contributions in quadrature.

The uncertainties in the B and B^* masses lead to correlated uncertainties in E_{cm} and in the E_{cm} spread. The corresponding contributions are determined by varying the masses by their uncertainties and repeating the analysis. The uncertainties in E_{cm} are shown in Table 9. They are roughly independent of the energy. The total uncertainty is calculated as the sum in quadrature of the various contributions. The uncertainties in the E_{cm} spread are relatively small; their total contributions are shown in Table 6.

Table 9: Systematic uncertainty in E_{cm} due to uncertainties in the B and B^* masses.

Source	Systematic uncertainty (MeV)
$m(B^+) = (5279.25 \pm 0.26) \text{ MeV}/c^2$	± 0.29
$m(B^0) = (5279.63 \pm 0.20) \text{ MeV}/c^2$	± 0.18
$m(B^*) - m(B) = (45.42 \pm 0.26) \text{ MeV}/c^2$	± 0.37
Total	± 0.50

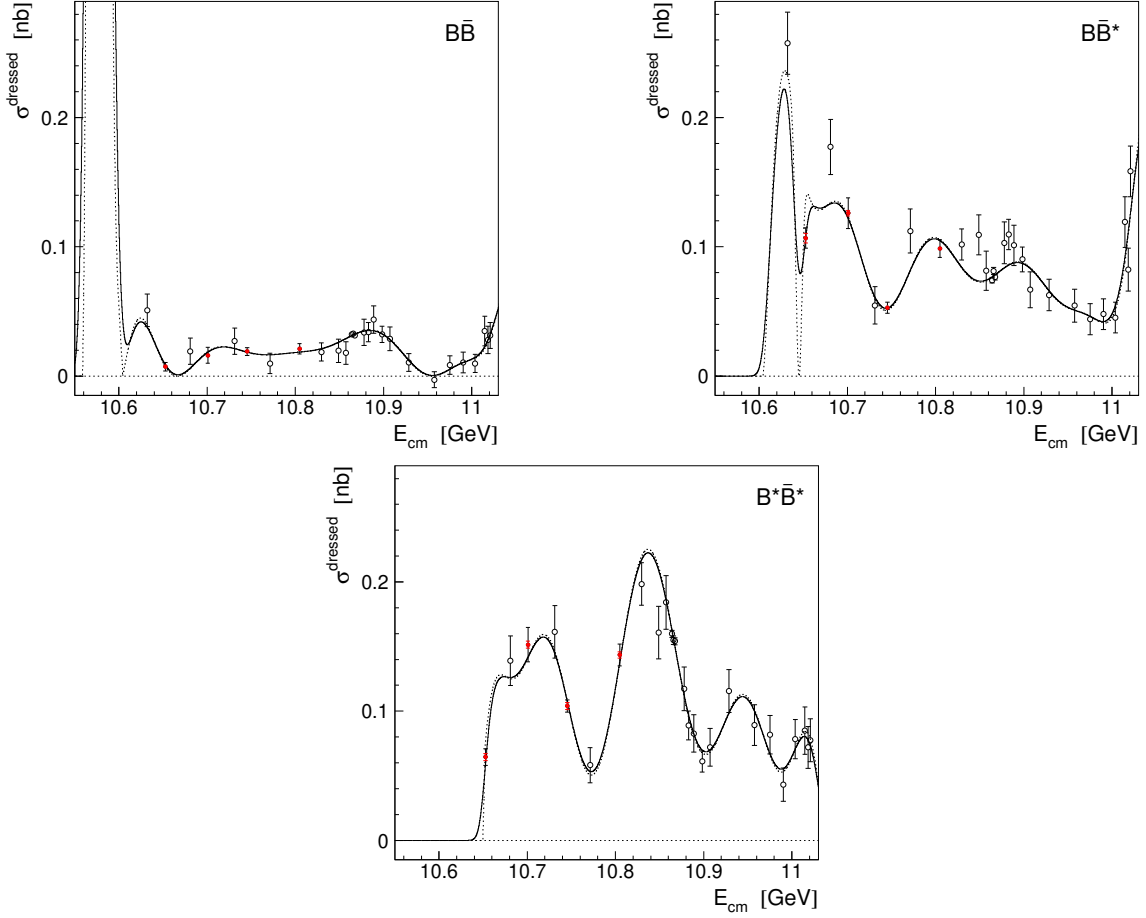


Figure 12: Energy dependence of the $e^+e^- \rightarrow B\bar{B}$ (left), $B\bar{B}^*$ (right), and $B^*\bar{B}^*$ (bottom) cross sections. Red filled and black open circles show the Belle II and Belle measurements, respectively. In the Belle II results, black error bars show statistical uncertainties, red error bars show uncorrelated systematic uncertainties. (On six out of the twelve points, the systematic uncertainties are smaller than the size of the red filled circle, and thus not visible.) The solid curves show the default fit result; the dashed curves show the fit function before the convolution used to account for the E_{cm} spread.

7 Discussion and summary

In Fig. 14 we show the sum of the exclusive $B\bar{B}$, $B\bar{B}^*$, and $B^*\bar{B}^*$ cross sections measured in this work and in the Belle experiment [8], superimposed on the total $b\bar{b}$ dressed cross section [7]. The sum of measurements performed in this work agrees well with the total cross section up to $E_{\text{cm}} = 10.84$ GeV. The deviation at higher energy is presumably due to the contribution of B_s^0 mesons, multibody final states $B^{(*)}\bar{B}^{(*)}\pi(\pi)$, and production of bottomonia in association with light hadrons.

The results of the fit to the Belle and Belle II points, and a separate fit to the Belle points only, are shown in Fig. 15. As measurements of the dressed cross section rely on the energy dependence of the cross section as an input, and our measurements have improved

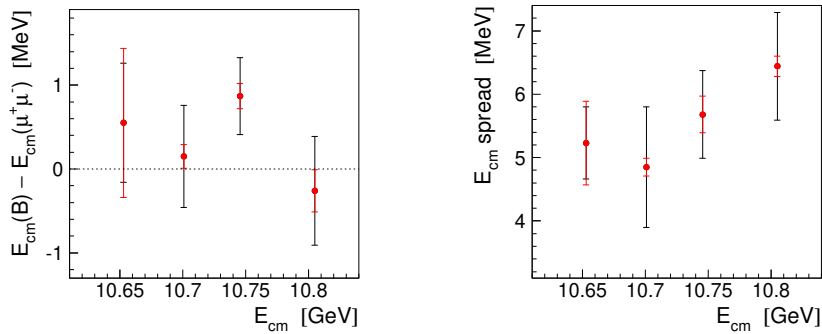


Figure 13: Measurements of the energy difference $E_{\text{cm}}(B) - E_{\text{cm}}(\mu^+\mu^-)$ (left) and the E_{cm} spread (right) at various energies. Black error bars show statistical uncertainties, red error bars show uncorrelated systematic uncertainties.

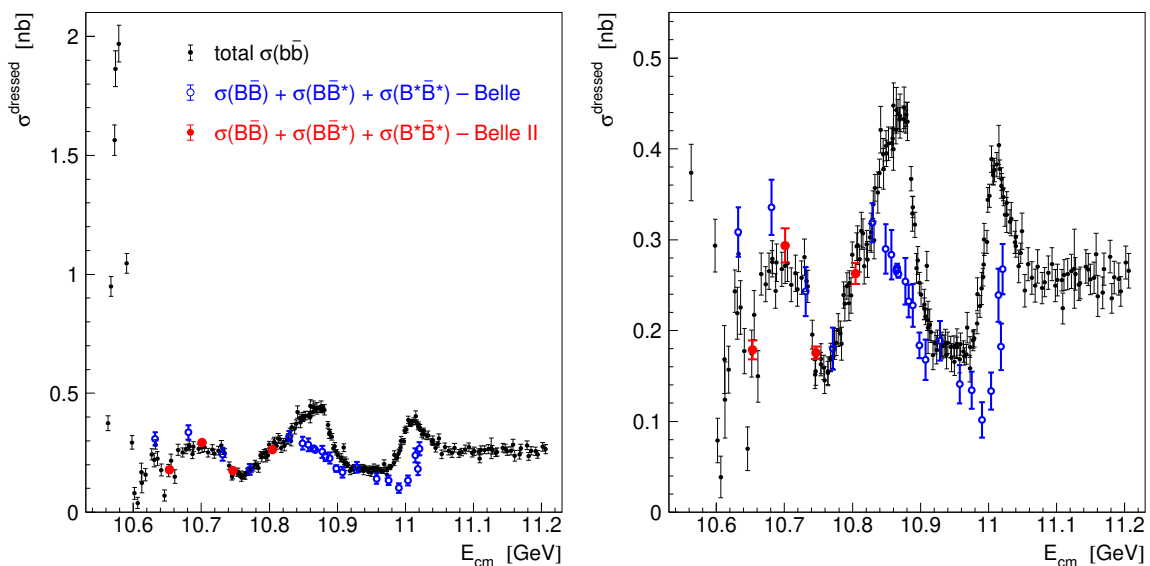


Figure 14: Energy dependence of the total $b\bar{b}$ dressed cross section obtained in Ref. [7] from the visible cross sections measured by Belle [31], and BaBar [26] (black circles) and the sum of the exclusive $B\bar{B}$, $B\bar{B}^*$, and $B^*\bar{B}^*$ cross sections measured by Belle [8] (open blue circles) and in this work (filled red circles). The right panel shows the low cross-section region with an expanded scale.

the knowledge of this energy dependence, the Belle measurements may be shifted as a result. However, we find that the shifts are negligibly small compared to the corresponding uncertainties.

A new and unexpected observation of this analysis is that the $e^+e^- \rightarrow B^*\bar{B}^*$ cross section increases very rapidly just above the threshold. The energy of the nearby scan point $E_{\text{cm}} = (10653.30 \pm 1.14)$ MeV is only (2.96 ± 1.52) MeV higher than the $B^{*0}\bar{B}^{*0}$ threshold and only (4.78 ± 1.47) MeV higher than the $B^{*+}B^{*-}$ threshold; these differences are less than the E_{cm} spread of $\sigma = (5.23 \pm 0.89)$ MeV. The large observed value of the $B^*\bar{B}^*$

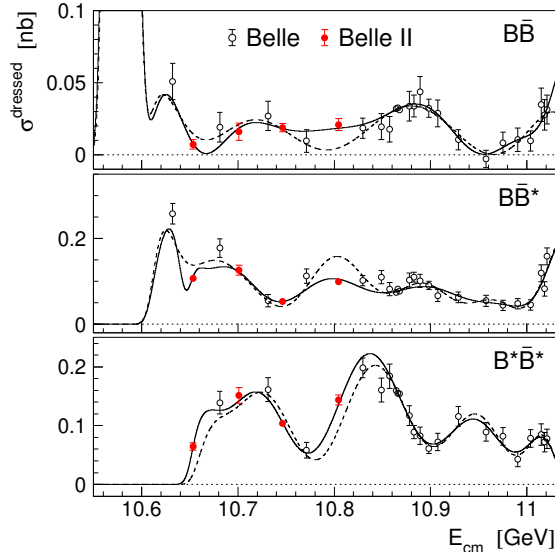


Figure 15: Energy dependence of the cross sections: $e^+e^- \rightarrow B\bar{B}$ (top), $B\bar{B}^*$ (middle) and $B^*\bar{B}^*$ (bottom). Symbols and curves have the same meaning as in Fig. 9, except that dashed curves show the result of the fit to the Belle points only [8].

cross section at this scan point is especially surprising since phase space in the reaction $e^+e^- \rightarrow B^*\bar{B}^*$ grows as the $3/2$ power of the difference between the beam energy and the threshold energy, and thus the derivative of the cross section of this process must vanish at the threshold. Hence, we conclude that the amplitude of the process under consideration increases rapidly towards the threshold. This phenomenon can be explained by the presence of a $B^*\bar{B}^*$ molecular state near the $B^*\bar{B}^*$ threshold. Such a state could be bound or virtual; the B^* and \bar{B}^* mesons are in relative P-wave. There is a similar phenomenon near $D^*\bar{D}^*$ threshold, which was explained in Ref. [32] by the presence of a $D^*\bar{D}^*$ molecule.

The existence of a $B^*\bar{B}^*$ molecule would also provide a natural explanation for the narrow dip in the $e^+e^- \rightarrow B\bar{B}^*$ cross section near the $B^*\bar{B}^*$ threshold (Fig. 9), as destructive interference between $e^+e^- \rightarrow B\bar{B}^*$ and the $e^+e^- \rightarrow B^*\bar{B}^* \rightarrow B\bar{B}^*$ rescattering process.³ One can expect that such a complex behavior of the cross sections near the $B^*\bar{B}^*$ threshold might lead to nontrivial effects, such as a large violation of isospin symmetry, enhancement of inelastic processes such as $e^+e^- \rightarrow \Upsilon(nS)\pi^+\pi^-$ and $h_b(1P)\eta$, and violation of heavy-quark spin symmetry due to the interaction of B mesons in the final state [34].⁴ Further study of this energy region with larger samples should make it possible to confirm or refute the existence of such a near-threshold resonance.

In summary, we report measurements of the $e^+e^- \rightarrow B\bar{B}$, $e^+e^- \rightarrow B\bar{B}^*$, and $e^+e^- \rightarrow B^*\bar{B}^*$ cross sections at four energies between 10.65 and 10.80 GeV using Belle II data with a total integrated luminosity of 19.7 fb^{-1} (Table 8). The obtained two-body cross sections at these energies are consistent with the earlier results of Belle [8], and provide significant

³Alternatively, the dip may arise from a node in the $\Upsilon(4S)$ wave function [33].

⁴Phenomenological analysis [35] of the preliminary results [36] of this work confirms the presence of a molecular state near the $B^*\bar{B}^*$ threshold.

additional information. These results can be used in coupled-channel analysis of energy-scan data to extract parameters of the highly excited Υ states, in particular, of the recently observed $\Upsilon(10753)$ state. We find that the $e^+e^- \rightarrow B^*\bar{B}^*$ cross section increases very rapidly above the corresponding threshold, which might indicate the presence of a $B^*\bar{B}^*$ molecular state near the threshold.

8 Acknowledgements

This work, based on data collected using the Belle II detector, which was built and commissioned prior to March 2019, was supported by Higher Education and Science Committee of the Republic of Armenia Grant No. 23LCG-1C011; Australian Research Council and Research Grants No. DP200101792, No. DP210101900, No. DP210102831, No. DE220100462, No. LE210100098, and No. LE230100085; Austrian Federal Ministry of Education, Science and Research, Austrian Science Fund No. P 34529, No. J 4731, No. J 4625, and No. M 3153, and Horizon 2020 ERC Starting Grant No. 947006 “InterLeptons”; Natural Sciences and Engineering Research Council of Canada, Compute Canada and CANARIE; National Key R&D Program of China under Contract No. 2022YFA1601903, National Natural Science Foundation of China and Research Grants No. 11575017, No. 11761141009, No. 11705209, No. 11975076, No. 12135005, No. 12150004, No. 12161141008, and No. 12175041, and Shandong Provincial Natural Science Foundation Project ZR2022JQ02; the Czech Science Foundation Grant No. 22-18469S and Charles University Grant Agency project No. 246122; European Research Council, Seventh Framework PIEF-GA-2013-622527, Horizon 2020 ERC-Advanced Grants No. 267104 and No. 884719, Horizon 2020 ERC-Consolidator Grant No. 819127, Horizon 2020 Marie Skłodowska-Curie Grant Agreement No. 700525 “NIOBE” and No. 101026516, and Horizon 2020 Marie Skłodowska-Curie RISE project JENNIFER2 Grant Agreement No. 822070 (European grants); L’Institut National de Physique Nucléaire et de Physique des Particules (IN2P3) du CNRS and L’Agence Nationale de la Recherche (ANR) under grant ANR-21-CE31-0009 (France); BMBF, DFG, HGF, MPG, and AvH Foundation (Germany); Department of Atomic Energy under Project Identification No. RTI 4002, Department of Science and Technology, and UPES SEED funding programs No. UPES/R&D-SEED-INFRA/17052023/01 and No. UPES/R&D-SOE/20062022/06 (India); Israel Science Foundation Grant No. 2476/17, U.S.-Israel Binational Science Foundation Grant No. 2016113, and Israel Ministry of Science Grant No. 3-16543; Istituto Nazionale di Fisica Nucleare and the Research Grants BELLE2; Japan Society for the Promotion of Science, Grant-in-Aid for Scientific Research Grants No. 16H03968, No. 16H03993, No. 16H06492, No. 16K05323, No. 17H01133, No. 17H05405, No. 18K03621, No. 18H03710, No. 18H05226, No. 19H00682, No. 20H05850, No. 20H05858, No. 22H00144, No. 22K14056, No. 22K21347, No. 23H05433, No. 26220706, and No. 26400255, and the Ministry of Education, Culture, Sports, Science, and Technology (MEXT) of Japan; National Research Foundation (NRF) of Korea Grants No. 2016R1D1A1B02012900, No. 2018R1A2B-3003643, No. 2018R1A6A1A06024970, No. 2019R1I1A3A01058933, No. 2021R1A6A1A-03043957, No. 2021R1F1A1060423, No. 2021R1F1A1064008, No. 2022R1A2C1003993, and No. RS-2022-00197659, Radiation Science Research Institute, Foreign Large-Size Research

Facility Application Supporting project, the Global Science Experimental Data Hub Center of the Korea Institute of Science and Technology Information and KREONET/GLORIAD; Universiti Malaya RU grant, Akademi Sains Malaysia, and Ministry of Education Malaysia; Frontiers of Science Program Contracts No. FOINS-296, No. CB-221329, No. CB-236394, No. CB-254409, and No. CB-180023, and SEP-CINVESTAV Research Grant No. 237 (Mexico); the Polish Ministry of Science and Higher Education and the National Science Center; the Ministry of Science and Higher Education of the Russian Federation and the HSE University Basic Research Program, Moscow; University of Tabuk Research Grants No. S-0256-1438 and No. S-0280-1439 (Saudi Arabia); Slovenian Research Agency and Research Grants No. J1-9124 and No. P1-0135; Agencia Estatal de Investigacion, Spain Grant No. RYC2020-029875-I and Generalitat Valenciana, Spain Grant No. CIDEGENT/2018/020; The Knut and Alice Wallenberg Foundation (Sweden), Contracts No. 2021.0174 and No. 2021.0299; National Science and Technology Council, and Ministry of Education (Taiwan); Thailand Center of Excellence in Physics; TUBITAK ULAKBIM (Turkey); National Research Foundation of Ukraine, Project No. 2020.02/0257, and Ministry of Education and Science of Ukraine; the U.S. National Science Foundation and Research Grants No. PHY-1913789 and No. PHY-2111604, and the U.S. Department of Energy and Research Awards No. DE-AC06-76RLO1830, No. DE-SC0007983, No. DE-SC0009824, No. DE-SC0009973, No. DE-SC0010007, No. DE-SC0010073, No. DE-SC0010118, No. DE-SC0010504, No. DE-SC0011784, No. DE-SC0012704, No. DE-SC0019230, No. DE-SC0021274, No. DE-SC0021616, No. DE-SC0022350, No. DE-SC0023470; and the Vietnam Academy of Science and Technology (VAST) under Grants No. NVCC.05.12/22-23 and No. DL0000.02/24-25.

These acknowledgements are not to be interpreted as an endorsement of any statement made by any of our institutes, funding agencies, governments, or their representatives.

We thank the SuperKEKB team for delivering high-luminosity collisions; the KEK cryogenics group for the efficient operation of the detector solenoid magnet; the KEK Computer Research Center for on-site computing support; the NII for SINET6 network support; and the raw-data centers hosted by BNL, DESY, GridKa, IN2P3, INFN, and the University of Victoria.

References

- [1] A. E. Bondar, R. V. Mizuk, and M. B. Voloshin, “Bottomonium-like states: Physics case for energy scan above the $B\bar{B}$ threshold at Belle II,” *Mod. Phys. Lett. A* **32**, 1750025 (2017).
- [2] C. Meng and K. T. Chao, “Scalar resonance contributions to the dipion transition rates of $\Upsilon(4S, 5S)$ in the re-scattering model,” *Phys. Rev. D* **77**, 074003 (2008).
- [3] Y. A. Simonov and A. I. Veselov, “Strong decays and dipion transitions of $\Upsilon(5S)$,” *Phys. Lett. B* **671**, 55 (2009).
- [4] R. Kaiser, A. V. Manohar, and T. Mehen, “Isospin violation in $e^+e^- \rightarrow B\bar{B}$,” *Phys. Rev. Lett.* **90**, 142001 (2003).
- [5] M. B. Voloshin, “Heavy quark spin symmetry breaking in near-threshold $J^{PC} = 1^{--}$ quarkonium-like resonances,” *Phys. Rev. D* **85**, 034024 (2012).

- [6] R. Mizuk *et al.* [Belle Collaboration], “Observation of a new structure near 10.75 GeV in the energy dependence of the $e^+e^- \rightarrow \Upsilon(nS)\pi^+\pi^-$ ($n = 1, 2, 3$) cross sections,” *JHEP* **10** (2019) 220.
- [7] X. K. Dong, X. H. Mo, P. Wang, and C. Z. Yuan, “Hadronic cross section of e^+e^- annihilation at bottomonium energy region,” *Chin. Phys. C* **44**, 083001 (2020).
- [8] R. Mizuk *et al.* [Belle Collaboration], “Measurement of the energy dependence of the $e^+e^- \rightarrow B\bar{B}, B\bar{B}^*$ and $B^*\bar{B}^*$ exclusive cross sections,” *JHEP* **06** (2021) 137.
- [9] N. Hüsken, R. E. Mitchell, and E. S. Swanson, “K-matrix analysis of e^+e^- annihilation in the bottomonium region,” *Phys. Rev. D* **106**, 094013 (2022).
- [10] I. Adachi *et al.* [Belle II Collaboration], “Study of $\Upsilon(10753)$ decays to $\pi^+\pi^-\Upsilon(nS)$ final states at Belle II,” [arXiv:2401.12021 [hep-ex]], submitted to *JHEP*.
- [11] I. Adachi *et al.* [Belle II Collaboration], “Observation of $e^+e^- \rightarrow \omega\chi_{bJ}(1P)$ and search for $X_b \rightarrow \omega\Upsilon(1S)$ at \sqrt{s} near 10.75 GeV,” *Phys. Rev. Lett.* **130**, 091902 (2023).
- [12] I. Adachi *et al.* [Belle II Collaboration], “Search for the $e^+e^- \rightarrow \eta_b(1S)\omega$ and $e^+e^- \rightarrow \chi_{b0}(1P)\omega$ processes at $\sqrt{s} = 10.745$ GeV,” *Phys. Rev. D* **109**, 072013 (2024).
- [13] T. Keck *et al.*, “The Full Event Interpretation: An Exclusive Tagging Algorithm for the Belle II Experiment,” *Comput. Softw. Big Sci.* **3**, 6 (2019).
- [14] T. Abe *et al.* [Belle II Collaboration], “Belle II Technical Design Report,” [arXiv:1011.0352 [physics.ins-det]].
- [15] K. Akai *et al.* [SuperKEKB], “SuperKEKB Collider,” *Nucl. Instrum. Meth. A* **907**, 188 (2018).
- [16] D. J. Lange, “The EvtGen particle decay simulation package,” *Nucl. Instrum. Meth. A* **462**, 152 (2001).
- [17] S. Jadach, B. F. L. Ward, and Z. Was, “The Precision Monte Carlo event generator KK for two fermion final states in e^+e^- collisions,” *Comput. Phys. Commun.* **130**, 260 (2000).
- [18] T. Sjöstrand, S. Ask, J. R. Christiansen, R. Corke, N. Desai, P. Ilten, S. Mrenna, S. Prestel, C. O. Rasmussen, and P. Z. Skands, “An introduction to PYTHIA 8.2,” *Comput. Phys. Commun.* **191**, 159 (2015).
- [19] E. Barberio, B. van Eijk and Z. Was, “PHOTOS: A Universal Monte Carlo for QED radiative corrections in decays,” *Comput. Phys. Commun.* **66**, 115 (1991).
- [20] S. Agostinelli *et al.*, “GEANT4 – a simulation toolkit,” *Nucl. Instrum. Meth. A* **506**, 250 (2003).
- [21] T. Kuhr *et al.* [Belle II Framework Software Group], “The Belle II Core Software,” *Comput. Softw. Big Sci.* **3**, 1 (2019).
- [22] E. Kou *et al.*, “The Belle II Physics Book,” *PTEP* **2019**, 123C01 (2019) [erratum: *PTEP* **2020**, 029201 (2020)].
- [23] T. Keck, “FastBDT: A Speed-Optimized Multivariate Classification Algorithm for the Belle II Experiment,” *Comput. Softw. Big Sci.* **1**, 2 (2017).
- [24] G. C. Fox and S. Wolfram, “Observables for the Analysis of Event Shapes in e^+e^- Annihilation and Other Processes,” *Phys. Rev. Lett.* **41**, 1581 (1978).

- [25] E.A. Kuraev and V.S. Fadin, “On Radiative Corrections to e^+e^- Single Photon Annihilation at High-Energy,” *Sov. J. Nucl. Phys.* **41**, 466 (1985).
- [26] B. Aubert *et al.* [BaBar Collaboration], “Measurement of the $e^+e^- \rightarrow b\bar{b}$ cross section between $\sqrt{s} = 10.54$ GeV and 11.20 GeV,” *Phys. Rev. Lett.* **102**, 012001 (2009).
- [27] R. L. Workman *et al.* [Particle Data Group], “Review of Particle Physics,” *PTEP* **2022**, 083C01 (2022) and 2023 updates.
- [28] B. Aubert *et al.* [BaBar Collaboration], “Measurement of the Mass Difference $m(B^0) - m(B^+)$,” *Phys. Rev. D* **78**, 011103 (2008).
- [29] A. E. Bondar, A. I. Milstein, R. V. Mizuk, and S. G. Salnikov, “Effects of isospin violation in the $e^+e^- \rightarrow B^{(*)}\bar{B}^{(*)}$ cross sections,” *JHEP* **05** (2022) 170.
- [30] F. Abudinén *et al.* [Belle II Collaboration], “Measurement of the integrated luminosity of the Phase 2 data of the Belle II experiment,” *Chin. Phys. C* **44**, 021001 (2020).
- [31] D. Santel *et al.* [Belle Collaboration], “Measurements of the $\Upsilon(10860)$ and $\Upsilon(11020)$ resonances via $\sigma(e^+e^- \rightarrow \Upsilon(nS)\pi^+\pi^-)$,” *Phys. Rev. D* **93**, 011101 (2016).
- [32] S. Dubynskiy and M. B. Voloshin, “Possible new resonance at the $D^*\bar{D}^*$ threshold in e^+e^- annihilation,” *Mod. Phys. Lett. A* **21**, 2779 (2006).
- [33] S. Ono, A. I. Sanda and N. A. Tornqvist, “ B Meson Production Between the $\Upsilon(4S)$ and $\Upsilon(6S)$ and the Possibility of Detecting $B\bar{B}$ Mixing,” *Phys. Rev. D* **34**, 186 (1986).
- [34] X. Li and M. B. Voloshin, “Mixing of partial waves near $B^*\bar{B}^*$ threshold in e^+e^- annihilation,” *Phys. Rev. D* **87**, 094033 (2013).
- [35] S. G. Salnikov, A. E. Bondar and A. I. Milstein, “Coupled channels and production of near-threshold $B^{(*)}\bar{B}^{(*)}$ resonances in e^+e^- annihilation,” *Nucl. Phys. A* **1041**, 122764, (2024).
- [36] M. Bertemes, “Quarkonium and charm physics at Belle II,” *QCD and High Energy Interactions (LaThuile, 2023)*.

A Reconstruction channels of B and D mesons

The channels used to reconstruct B and D mesons are listed in Tables 10 and 11. The sum of the corresponding branching fractions is 7.2% for B^+ , 6.1% for B^0 , 44.6% for D^0 , 28.6% for D^+ , and 17.2% for D_s^+ .

Table 10: Decay channels of B^+ and B^0 mesons used in the FEI.

$B^+ \rightarrow$	$B^0 \rightarrow$
$\bar{D}^0 \pi^+$	$D^- \pi^+$
$\bar{D}^0 \pi^+ \pi^+ \pi^-$	$D^- \pi^+ \pi^+ \pi^-$
$\bar{D}^{*0} \pi^+$	$D^{*-} \pi^+$
$\bar{D}^{*0} \pi^+ \pi^+ \pi^-$	$D^{*-} \pi^+ \pi^+ \pi^-$
$D_s^+ \bar{D}^0$	$D_s^+ D^-$
$D_s^{*+} \bar{D}^0$	$D_s^{*+} D^-$
$D_s^+ \bar{D}^{*0}$	$D_s^+ D^{*-}$
$D_s^{*+} \bar{D}^{*0}$	$D_s^{*+} D^{*-}$
$J/\psi K^+$	$J/\psi K_S^0$
$J/\psi K_S^0 \pi^+$	$J/\psi K^+ \pi^-$
$J/\psi K^+ \pi^+ \pi^-$	
$D^- \pi^+ \pi^+$	$D^{*-} K^+ K^- \pi^+$
$D^{*-} \pi^+ \pi^+$	

Table 11: Decay channels of D^0 , D^+ and D_s^+ mesons used in the FEI.

$D^0 \rightarrow$	$D^+ \rightarrow$	$D_s^+ \rightarrow$
$K^- \pi^+$	$K^- \pi^+ \pi^+$	$K^+ K^- \pi^+$
$K^- \pi^+ \pi^0$	$K^- \pi^+ \pi^+ \pi^0$	$K^+ K_S^0$
$K^- \pi^+ \pi^+ \pi^-$	$K_S^0 \pi^+$	$K^+ K^- \pi^+ \pi^0$
$K_S^0 \pi^+ \pi^-$	$K_S^0 \pi^+ \pi^0$	$K^+ K_S^0 \pi^+ \pi^-$
$K_S^0 \pi^+ \pi^- \pi^0$	$K_S^0 \pi^+ \pi^+ \pi^-$	$K^- K_S^0 \pi^+ \pi^+$
$K^+ K^-$	$K^+ K^- \pi^+$	$K^+ K^- \pi^+ \pi^+ \pi^-$
$K^+ K^- K_S^0$		$K^+ \pi^+ \pi^-$
		$\pi^+ \pi^+ \pi^-$